

# Spectroscopy of a Sample of Unidentified Gamma-ray Fermi Sources

Alberto Ulgiati<sup>1,2\*</sup>, Simona Paiano<sup>1†</sup>, Aldo Treves<sup>3,4</sup>, Renato Falomo<sup>5</sup>, Boris Sbarufatti<sup>4</sup>, Fabio Pintore<sup>1</sup>, Thomas D. Russell<sup>1</sup>, Giancarlo Cusumano<sup>1</sup>

<sup>1</sup>INAF - IASF Palermo, via Ugo La Malfa, 153, I-90146, Palermo, Italy

<sup>2</sup>Università degli Studi di Palermo, Dipartimento di Fisica e Chimica, via Archirafi 36, I-90123 Palermo, Italy

<sup>3</sup>Università dell'Insubria, via Valsabbia, 22100, Como, Italy

<sup>4</sup>INAF - Osservatorio Astronomico di Brera, via Bianchi 46, I-23807, Merate (Lecco), Italy

<sup>5</sup>INAF - Osservatorio Astronomico di Padova, vicolo dell'Osservatorio 5, I-35122, Padova, Italy

Accepted: 2024 February 19; Received 2024 February 5; in original form 2023 October 24.

## ABSTRACT

The fourth-DR3 version (4FGL-DR3) of the Fermi/LAT catalogue of  $\gamma$ -ray sources contains  $\sim 1000$  objects at a galactic latitude  $|b| > 10^\circ$  which are not identified with an optical counterpart (UGS). We performed a systematic study of these sources, focusing on 190 objects that have a unique X-ray counterpart in the available *Swift*/XRT observations. Optical counterparts are then selected, and for 33 sources optical spectra were found in the literature. We found that 21 can be classified as BL Lac objects. Among these we were able to provide the redshift for 8 of them while for 2 others we established a lower limit to the redshift by detecting intervening absorption. The other 12 objects display optical spectra with prominent emission lines ( $0.036 < z < 1.65$ ). These spectra are characterized by both broad and narrow emission lines with the exception of 3 sources. One of them displays only broad emission lines, while the other two exclusively exhibit narrow lines. On the basis of the radio/optical flux ratio, all BL Lac objects in this study are radio loud. Four sources out of the 12 with prominent emission lines can be classified as radio loud, while at least 5 of the 12 sources with prominent lines are radio quiet. This is somewhat unexpected comparing with the radio-loudness distribution of the 4FGL-associated blazars.

**Key words:** galaxies: active - galaxies: distances and redshifts - quasars: emission lines - BL Lacertae objects: general - gamma-rays: galaxies - galaxies: Seyfert

## 1 INTRODUCTION

In the last 15 years the *Fermi* satellite contributed dramatically to the progress of high-energy astrophysics. The third version of the Fermi-LAT Fourth Source Catalogue (4FGL-DR3, Abdollahi et al. 2020, 2022), based on 12 years of observations and containing 6659  $\gamma$ -ray detections, was released in June 2022.

About 4500 sources are associated or identified with targets at other wavelengths thanks to a positional overlap in the sky, measurements of correlated variability at other wavelengths, and/or multi-wavelength spectral properties (Abdollahi et al. 2020, 2022). The majority of the *Fermi* extragalactic population (at  $|b| > 10^\circ$ ) belongs to the blazar class, radio jetted Active Galactic Nuclei (AGN) with relativistic jets oriented close to the line of sight of the observer. Therefore, the  $\gamma$ -rays band presents an efficient and suitable energy band to detect this class of sources.

Blazar radiation, from radio to  $\gamma$ -ray band, is dominated by non-thermal emission and the typical Spectral Energy Distribution (SED) exhibits a doubled-bump shape. The first low energy peak, ranging from radio to X-rays energy band, is due to a synchrotron emission from relativistic electrons, while for the second one at high energy

(in the MeV - TeV range) the origin remains still under debate and several scenarios are proposed in the framework of hadronic and/or leptonic models (e.g. Cerruti et al. 2011; Costamante et al. 2018; Rodrigues et al. 2019; Gao et al. 2019; Cerruti 2020).

Based on the properties of their optical spectra, blazars are divided in two main classes: i) Flat Spectrum Radio Quasars (FSRQs) characterised by prominent emission lines and ii) BL Lacertae objects (BLL) for which the spectral features are very weak or even absent (e.g. Falomo, Pian, & Treves 2014). This implies that for a large fraction of BLL the redshift is unknown or highly uncertain, making their characterization in terms of physical properties and modelling quite difficult.

In any case, the firm classification of the Fermi sources requires spectroscopy of the optical counterpart. After the release of the first Fermi catalogs and subsequent versions, a number of optical campaigns were activated. One of the first substantial contributions came from Shaw et al. (2012, 2013) that collected optical spectra of  $\sim 500$  blazars reported in the *Fermi* catalogs. The results of the search on blazar candidates proposed on the basis of the colours of the infrared (IR) counterparts in the Wide-field Infrared Survey Explorer (WISE) survey and subsequent optical spectroscopy were presented by D'Abrusco et al. (2013), Massaro et al. (2015, 2016) and references therein, who found  $\sim 600$  blazar candidates and established the blazar nature for  $\sim 200$  of them.

\* E-mail: alberto.ulgiati@inaf.it

† E-mail: simona.paiano@inaf.it

Our group has carried out several campaigns of optical spectroscopy (some of them still on-going) and, in particular, we focused on the analysis of optical spectra of various samples of GeV-TeV blazars and neutrino candidate blazars, with the aim to determine their classification, the redshift and/or an upper limit of the redshift (see details in [Paiano et al. 2017a](#)). In particular [Paiano et al. \(2017a,b, 2020\)](#) analysed 87 Fermi BLL (or candidates) detected in the VHE band. In [Paiano et al. \(2021, 2023\)](#) and [Padovani et al. \(2022\)](#) optical spectroscopy of  $\sim 50$  blazars candidates to be the counterparts of IceCube neutrino events, is reported. From the analysis of these spectra, we derived the properties of the emission lines, crucial for the source characterization, and from the spectral decomposition of the continuum we estimated the properties of the host galaxy and the mass of the central super massive black hole. No significant spectral differences were found for this group of objects with respect to the rest of Fermi BLL.

A recent summary of spectroscopic observations on blazar *Fermi* sources can be found in [Paliya et al. \(2021\)](#).

About 25% of the extragalactic sources reported in the *Fermi* catalogue still remains unassociated, either due to the lack of X-ray and/or radio counterparts or because of multiple possible associations at other wavelengths can be found inside the positional error box (on average circles of about 6 arcmins of radius). These unassociated  $\gamma$ -ray sources (UGSs) represent a key component of the very high-energy sky. Their identification with lower energy counterparts and classification is crucial for population studies and the interpretation of the cosmic evolution of the gamma-ray sources (e.g. [Ajello et al. 2014](#); [Ghisellini et al. 2017](#)). UGSs may hide new blazars and/or new AGN classes emitting at GeV energies (as Narrow Line Seyfert-1 and Seyfert-like objects, for which only a few are known as  $\gamma$ -ray emitters). Moreover, since most UGSs have weaker  $\gamma$ -ray fluxes (on average  $\sim 2 \times 10^{-12}$  erg cm $^{-2}$  s $^{-1}$ ) than the identified sources (with an average flux of  $\sim 1.6 \times 10^{-11}$  erg cm $^{-2}$  s $^{-1}$ ) in the 100 MeV to 100 GeV range, they can represent a more distant extragalactic population, and/or lower luminosity sources.

Since 2015 we carried out a systematic study, using *Swift*/XRT images, with the aim of finding lower energy counterparts, with respect to the  $\gamma$ -ray energy band, of UGS based on available X-ray data that cover the  $\gamma$ -ray error-box (e.g. [Stephen et al. 2010](#); [Takahashi et al. 2012](#); [Acero et al. 2013](#); [Takeuchi et al. 2013](#); [Landi et al. 2015](#); [Paiano, Franceschini, & Stamerra 2017c](#); [Paiano et al. 2017d, 2019](#); [Kerby et al. 2021](#); [Kaur, Kerby, & Falcone 2023](#)).

To assess the nature of the source, we use optical spectroscopy available in the literature or obtained by our dedicated observation campaign using telescopes in the 8-10m class (such as Gran Telescopio Canarias and Large Binocular Telescope). This allows us to estimate or constrain the redshifts confirming the extragalactic nature of the proposed UGS counterparts. Moreover this yields crucial information to constrain the source emission, to determine the main physical parameters of the emitting region (as the nucleus luminosity and the nucleus-to-host ratio), of the host galaxy (morphology, size, and luminosity) and to shed light on the extreme physical processes, e.g. the neutrino production.

In previous papers ([Paiano et al. 2017d, 2019](#)), we studied a sample of 48 UGSs selected from the 2FGL and 3FGL catalogs and with at least one X-ray source detected inside the UGS error box. All sources exhibited an AGN optical spectrum (44 are BLLs, 1 QSO, 1 NLSy1 and 2 objects with a Seyfert 2 type spectrum).

In this work, we report the results of the association study for a first sample of 33 UGSs of the 4FGL-DR3 catalogue that have only one X-ray counterpart in the Fermi error ellipse and for which an optical spectrum is already available in literature or in public

surveys, providing details about the main spectral properties and the classification.

This paper is structured as follows: in Section 2, we describe our procedure of search for UGS counterparts and the sample of this work, in Section 3 we present the main results from the analysis of the optical spectra and multi-wavelength data, in the Section 4 we summarize and discuss the main properties of the sample in a multi-wavelength point of view, and finally in Section 5 we give notes on individual objects.

We adopted concordance cosmology (e.g. [Seehars et al. 2016](#)) assuming Hubble constant  $H_0 = 70$  km s $^{-1}$  Mpc $^{-1}$ , matter density  $\Omega_{m,0} = 0.3$ , and dark energy density  $\Omega_{\Lambda,0} = 0.7$ .

## 2 SEARCH FOR UGS COUNTERPARTS AND DEFINITION OF SAMPLE

### 2.1 Search for UGS counterparts

#### 2.1.1 X-ray band

Over the last 10 years, the *Swift* satellite has been involved in a campaign dedicated to the observation of UGSs with the XRT telescope ([Stroh & Falcone 2013](#); [Falcone, Stroh, & Pryal 2014](#)), and all data are available in the public archive<sup>1</sup>. We searched for UGS X-ray counterparts by selecting all the *Swift*/XRT data that cover the UGS positions in the field of view. A total of 697 (over a total of the 1125) high latitude ( $|b| > 10^\circ$ ) UGSs are covered by at least one *Swift*/XRT observation. For each of them we obtained an X-ray skymap covering a sky region of  $\sim 15$  arcmins (see an example in Fig. 1 and for the remaining sources see Appendix A1). We reduced all the available *Swift*/XRT observations with the on-line tool provided by the *Swift* consortium<sup>2</sup> ([Goad et al. 2007](#); [Evans et al. 2009, 2020](#)) that, for each given UGS, created a 0.3–10 keV stacked image and performed a source detection. We considered as X-ray sources detection having signal-to-noise (SNR)  $\geq 3.0$  inside the  $3\sigma$  *Fermi* positional error ellipses<sup>3</sup>. The online tool provides as output the source detection list, with the position<sup>4</sup> and the signal-to-noise ratio.

We find that 265 UGSs have at least one X-ray detection inside the  $\gamma$ -ray error box, and in particular 190 of them have only one possible X-ray counterpart inside the  $\gamma$ -ray error box, while the remaining 75 have multiple number of X-ray sources. These numbers obviously depends on the chosen significance of the X-ray detection.

#### 2.1.2 Radio band

Starting from the X-ray positions and error boxes (on average of the order of 4 arcsecs), we looked for radio and optical counterparts. We used two radio catalogs, provided by the Very Large Array Sky Survey (VLASS, [Gordon et al. 2021](#)) and the Rapid ASKAP Continuum Survey (RACS, [Hale et al. 2021](#)). Furthermore, we performed

<sup>1</sup> [https://www.swift.ac.uk/swift\\_portal/](https://www.swift.ac.uk/swift_portal/)

<sup>2</sup> [https://www.swift.ac.uk/user\\_objects/](https://www.swift.ac.uk/user_objects/)

<sup>3</sup> Note the two axes of the 4FGL-DR3 error ellipses at 95% confidence level have been increased by 50% in order to yield the  $\sim 99\%$  confidence level (see examples in Fig. A1).

<sup>4</sup> If data acquired with the UV and Optical Telescope (UVOT) on board of *Swift* are available, the on-line *Swift* analysis tool gives the enhanced position corrected for astrometry.

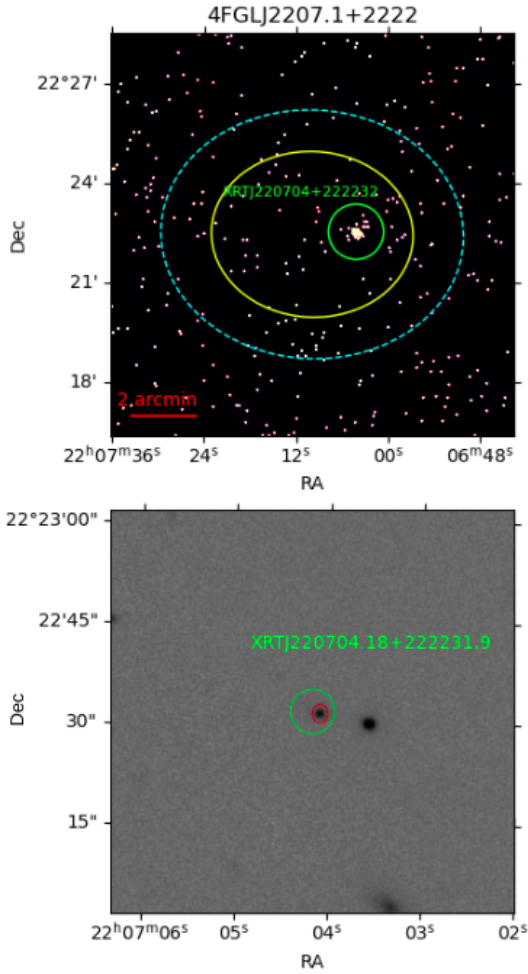


**Figure 1.** *Upper panel:* X-ray skymap of 4FGLJ2207.1+2222. The yellow and cyan ellipses are respectively the  $2\sigma$  and  $3\sigma$  *Fermi*  $\gamma$ -ray error regions. X-ray detection, found through *Swift*/XRT analysis, is reported in green. *Bottom panel:* Optical r-band PanSTARRs image of 4FGLJ2207.1+2222 counterpart. The green circle represent the error box of the X-ray counterpart and the red ellipses the error box of radio counterparts found within VLASS catalog.

a dedicated search<sup>5</sup> for any uncatalogued radio sources using public radio images provided through the LOw-Frequency ARray (LOFAR) Two-metre Sky Survey (LoTSS, Shimwell et al. 2022) in the northern hemisphere and RACS in the southern hemisphere. For those sources that have a marginal detection ( $\text{SNR} \leq 3\sigma$ ), that show an extended structure (non-circularly symmetric radio source) or no radio images are available in literature, we asked observations with the Australian Telescope Compact Array (ATCA). Full details on the ATCA program, will be presented in a future publication (Ugliati et al., in prep.). For the case of 4FGLJ2030.0–0310, the details are reported in the source notes (see Section 5).

<sup>5</sup> The radio detection was performed by applying two circular regions: one around the source (found through the search for the centroid, or in the absence of an obvious source on the position of the X-ray source) of size 10 arcsec, and the other in a region without of radio sources, of size 50 arcsec, to estimate the background. The ratio between the maximum flux in the source region and the rms of the background region gives the SNR of the detection.

### 2.1.3 Optical band

For the optical band, we searched counterparts using catalogues by the Sloan Digital Sky Survey (SDSS, Ahumada et al. 2020), the Panoramic Survey Telescope and Rapid Response System (PanSTARRS, Chambers et al. 2016) database, the Dark Energy Survey (DES, Abbott et al. 2021) and the United States Naval Observatory (USNO, Monet et al. 2003) survey (see an example in Fig. 1-bottom panel and for the remaining sources see Appendix B).

For 15 objects (with redshift  $< 0.5$ ) and/or with a substantial contribution from the host galaxies), we analysed the r-band images taken from the PANSTARRs, SDSS and DES database. We have used the AIDA software (Uslenghi & Falomo 2011) in order to separate the nuclear and host galaxy components and to determine the main photometric and morphological characteristics of the host galaxies (absolute magnitude, effective radius, and Sersic index  $n$ <sup>6</sup>).

## 2.2 Definition of the sample under consideration

The necessary step to probe the nature of the sources and to provide a classification is to study their optical spectra. Considering the UGSs with only one X-ray detection, we found that 33 objects have a X-ray counterpart which has already an optical spectrum in literature. For other  $\sim 60$  UGS counterparts, optical spectroscopic data from large telescopes (e.g. Large Binocular Telescope (LBT) and Gran Telescopio Canarias (GTC)) has been already granted to our group (Paiano et al., in prep.).

In this paper we report the main results for this sub-sample of 33 sources, obtained by the study of the X-ray images and the analysis of the literature spectrum, when available in ASCII or FITS format. The main information of the *Swift*/XRT observations and results of the X-ray analysis are summarized in Tab. 1. In Tab. 2 we list the multiwavelength counterparts of each UGS. In Appendix A we show the *Fermi* error boxes superimposed to the X-ray images of this sample. Appendix B contains the optical images (Fig. B2) taken from the PANSTARRs database (with the exception of two cases in which the images were taken from the Dark Energy Survey (DES) and NOIRLab Astro Data archives) with the overlay of the proposed X-ray and radio counterparts. Details of the multiwavelength study, including the X-ray and the optical skymaps for the entire UGS sample with at least one X-ray detection will be presented in Ugliati et al., (in prep.).

## 3 RESULTS

The available and downloaded optical spectra found in literature of our 33 UGS sample (see Table 3 for the references) are shown in Fig. 2. The spectra were dereddened for the Galaxy contribution, applying the extinction law by Cardelli, Clayton, & Mathis (1989) and assuming the E(B-V) values provided by the NASA/IPAC infrared science archive<sup>7</sup>. Note that for two objects (4FGLJ0023.6-4209 and 4FGLJ2030.0-0310) the spectra, taken from the 6dF survey, are not flux calibrated and dereddened. Although they are useful for the redshift determination, no information of the magnitude of the source and line luminosities can be derived.

<sup>6</sup> The surface brightness profile of a galaxy is described by the Sersic law:  $\frac{I_r}{I_e} = \exp(-b_n ((\frac{r}{R_e})^{\frac{1}{n}} - 1))$ . where  $I_e$  is the light intensity at the effective radius  $R_e$ , the major-axis effective radius encompassing half of the total flux of the source,  $n$  is the Sersic index and  $b_n$  a constant depending on  $n$ .

<sup>7</sup> <https://irsa.ipac.caltech.edu/applications/DUST/>

**Table 1.** X-ray info of the 33 UGSs with only one X-ray counterpart within the  $3\sigma$  Fermi error box

4FGL Name	$\gamma$ -ray significance ( $\sigma$ )	Swift exp. time (ks)	XRT counterpart	RA (J2000)	DEC (J2000)	X-ray positional error radius (")	X-ray significance ( $\sigma$ )
4FGLJ0023.6-4209	5.1	3.4	XRTJ002303.5-420509.6	5.76496	-42.08601	2.9	5.0
4FGLJ0112.0+3442	4.8	4.7	XRTJ011124.8+344154.1	17.85359	34.69837	4.7	4.0
4FGLJ0117.9+1430	6.1	6.6	XRTJ011804.7+143159.5	19.51996	14.53322	3.0	4.7
4FGLJ0202.7+3133	4.3	10.5	XRTJ020242.1+313211.3	30.67554	31.53649	2.5	10.3
4FGLJ0251.1-1830	11.0	7.7	XRTJ025111.7-183111.1	42.79877	-18.51976	2.7	8.9
4FGLJ0259.0+0552	23.2	4.9	XRTJ025857.5+055244.4	44.73982	5.87900	3.4	5.2
4FGLJ0641.4+3349	4.4	3.6	XRTJ064111.2+334502.0	100.29683	33.75056	3.7	13.8
4FGLJ0838.5+4013	4.1	3.9	XRTJ083902.9+401546.9	129.76240	40.26303	3.0	4.4
4FGLJ0938.8+5155	6.1	10.6	XRTJ093834.5+515454.7	144.64375	51.91522	6.1	3.8
4FGLJ1016.1-4247	12.8	6.1	XRTJ101620.7-424723.2	154.08659	-42.78978	2.7	8.6
4FGLJ1039.2+3258	9.8	5.1	XRTJ103852.1+325651.9	159.71738	32.94776	3.0	4.6
4FGLJ1049.8+2741	6.5	5.5	XRTJ104938.7+274212.0	162.41124	27.70335	2.9	5.8
4FGLJ1125.1+4811	4.5	50.5	XRTJ112526.0+480922.8	171.35839	48.15634	5.4	4.3
4FGLJ1131.6+4657	6.3	4.6	XRTJ113142.3+470009.2	172.92651	47.00256	2.6	6.0
4FGLJ1146.0-0638	13.5	3.3	XRTJ114600.8-063853.9	176.50361	-6.64831	3.1	6.7
4FGLJ1256.8+5329	5.6	5.6	XRTJ125630.5+533202.2	194.12725	53.53397	6.4	4.2
4FGLJ1308.7+0347	9.7	3.6	XRTJ130832.2+034405.3	197.13445	3.73483	4.0	5.5
4FGLJ1346.5+5330	10.3	3.9	XRTJ134545.1+533252.4	206.43811	53.54791	2.2	13.5
4FGLJ1410.7+7405	22.9	11.7	XRTJ141045.6+740509.8	212.69026	74.08608	7.2	4.5
4FGLJ1430.6+1543	4.8	1.6	XRTJ143057.9+154556.0	217.74133	15.76529	3.1	5.4
4FGLJ1535.9+3743	18.1	10.7	XRTJ153550.5+374056.8	233.96065	37.68245	4.6	4.1
4FGLJ1539.1+1008	5.6	6.2	XRTJ153848.5+101841.7	234.70214	10.31159	3.2	5.0
4FGLJ1544.9+3218	6.5	13.9	XRTJ154433.1+322148.5	236.13813	32.36349	2.6	10.1
4FGLJ1554.2+2008	10.6	8.2	XRTJ155424.1+201125.3	238.60069	20.19041	2.0	34.5
4FGLJ1555.3+2903	5.1	3.5	XRTJ155513.0+290328.0	238.80422	29.05779	3.5	10.9
4FGLJ1631.8+4144	8.0	3.7	XRTJ163146.8+414631.8	247.94510	41.77550	2.6	8.9
4FGLJ1648.7+4834	5.7	4.2	XRTJ164900.5+483409.1	252.25233	48.56921	2.8	5.7
4FGLJ2030.0-0310	4.5	4.5	XRTJ203014.3-030722.8	307.55974	-3.12276	2.8	11.0
4FGLJ2207.1+2222	7.5	4.8	XRTJ220704.1+222231.8	331.76740	22.37552	3.3	5.0
4FGLJ2240.3-5241	11.8	5.8	XRTJ224017.55-524112.3	340.07314	-52.68676	3.6	3.4
4FGLJ2317.7+2839	10.7	14.1	XRTJ231740.1+283955.4	349.41730	28.66540	5.8	4.3
4FGLJ2323.1+2040	6.2	3.3	XRTJ232320.30+203523.6	350.83459	20.58990	4.2	3.5
4FGLJ2353.2+3135	9.0	28.0	XRTJ235319.39+313616.9	358.3308	31.6047	3.5	8.2

**Note.** Column 1: 4FGL Name of the target; Column 2:  $\gamma$ -ray detection significance as reported in the 4FGL catalog; Column 3: *Swift*/XRT exposure time; Column 4: X-ray counterpart detected from our Swift/XRT analysis (Names report the acronym of the XRT detector plus the J2000 sexagesimal coordinates); Column 5-6: Coordinates of the proposed X-ray counterpart in degrees; Column 7: X-ray positional error radius in arcsecs; Column 8: Detection significance of the X-ray counterpart.

From the redshifts deduced from the analysis of the optical spectra and/or the presence of a power-law component (typical of the BLL), it was possible to assess the extragalactic nature of the sources.

For 20 out of 33 objects, clear spectral features are found that allow us to derive their redshift (see Table 3). We determine the position of the emission and absorption lines performing accurate search of the centroids, by computing the barycenter of each line after subtraction of the underlined continuum. The redshift is determined by comparing the found wavelength centroids of each line with the expected rest-frame wavelengths. After checking that all lines provide consistent results, we derived the final redshift from the average. 11 sources do not reveal intrinsic spectral features. For 7 sources, the optical spectrum exhibits absorption lines of the host galaxy stellar population (Ca II 3934,3968, G-band 4305, Mg I5175, and Na I 5893), 12 objects present only emission lines, and for one case (4FGLJ0112.0+3442) both emission and absorption lines are present.

We can classify 21 sources as BLL: 15 with spectra characterized by a power-law emission and another 6 with a strong signature

of the stellar population due to the host galaxy (labelled as galaxy-dominated BLL (BLG) in Table 3). Seven BLLs have their redshift determined through the detection of the host galaxy absorption lines. The redshifts are in the interval  $0.04 < z < 0.64$  and the average value is  $\langle z \rangle = 0.2 \pm 0.1$ , in agreement with the typical BLL redshift distribution (Padovani et al. 2017; Garofalo et al. 2019). For two BLLs, 4FGLJ0251.0-1830 (Paiano et al. 2019, for details) and 4FGLJ2353.0+3135 (see Fig. 2), we can detect only intervening absorption systems due to MgII 2899 that allow us to provide a spectroscopic redshift lower limit.

The spectra of the remaining 12 objects all have prominent emission lines (mainly CIII], MgII, [OII], H $\beta$ , [OIII], H $\alpha$ , [N II] and [SII]), most of them showing a type-1 spectrum with broad and narrow emission lines. One high redshift source ( $z \geq 1$ ) displays only broad emission lines. 4FGLJ0117.9+1430 can be classified as a Narrow Line Seyfert 1 (see details in Sec. 5), while the other 11 have a Seyfert/QSO-like spectrum.

From the *r*-band image decomposition analysis of the 15 ob-

**Table 2.** Multiwavelength counterparts proposed for the sample of 33 UGSs

4FGL Name	XRT counterpart	Radio counterpart	Optical counterpart	RA J2000	DEC J2000
4FGLJ0023.6-4209	XRTJ002303.5-420509.6	RACSJ002303.61-420509.57	DESJ002303.74-420508.4	5.765596	-42.08569
4FGLJ0112.0+3442	XRTJ011124.8+344154.1	VLASS1QLCIRJ011124.83+344154.5	SDSSJ011124.86+344154.6	17.853583	34.698500
4FGLJ0117.9+1430	XRTJ011804.7+143159.5	-	SDSSJ011804.83+143158.6	19.520125	14.532944
4FGLJ0202.7+3133	XRTJ020242.1+313211.3	VLASS1QLCIRJ020242.03+313211.0	SDSSJ020242.06+313210.9	19.520125	14.532944
4FGLJ0251.1-1830	XRTJ025111.7-183111.1	VLASS1QLCIRJ025111.53-183112.3	PANJ025111.53-183112.7	42.798000	-18.520167
4FGLJ0259.0+0552	XRTJ025857.5+055244.4	VLASS1QLCIRJ025857.55+055244.0	SDSSJ025857.55+055243.9	44.739792	5.878861
4FGLJ0641.4+3349	XRTJ064111.24+334502.0	VLASS1QLCIRJ064111.20+334459.6	PANJ064111.22+334459.7	100.296750	33.749917
4FGLJ0838.5+4013	XRTJ083902.9+401546.9	VLASS1QLCIRJ083903.07+401545.6	SDSSJ083903.08+401545.6	129.762833	40.262667
4FGLJ0938.8+5155	XRTJ093834.5+515454.7	LoTSS093834.68+515451.8	SDSSJ093834.72+515452.3	144.644667	51.914528
4FGLJ1016.1-4247	XRTJ101620.7-424723.2	ATCAJ101620.76-424723.1	USNOJ101620.67-424722.6	154.086125	-42.789611
4FGLJ1039.2+3258	XRTJ103852.1+325651.9	VLASS1QLCIRJ103852.17+325651.9	SDSSJ103852.17+325651.6	159.717375	32.947667
4FGLJ1049.8+2741	XRTJ104938.7+274212.0	VLASS1QLCIRJ104938.81+274213.1	SDSSJ104938.79+274213.0	162.411625	27.703611
4FGLJ1125.1+4811	XRTJ112526.0+480922.8	-	SDSSJ112526.27+480922.0	171.359458	48.156111
4FGLJ1131.6+4657	XRTJ113142.3+470009.2	VLASS1QLCIRJ113142.36+470009.4	SDSSJ113142.27+470008.6	172.926125	47.002389
4FGLJ1146.0-0638	XRTJ114600.8-063853.9	VLASS1QLCIRJ114600.87-063854.5	USNOB1-0833-0250645	176.504000	-6.648556
4FGLJ1256.8+5329	XRTJ125630.5+533202.2	-	SDSSJ125630.43+533204.3	194.126792	53.534528
4FGLJ1308.7+0347	XRTJ130832.2+034405.3	-	SDSSJ130832.10+034403.9	197.133750	3.734417
4FGLJ1346.5+5330	XRTJ134545.1+533252.4	VLASS1QLCIRJ134545.34+533252.1	SDSSJ134545.36+533252.3	206.439000	53.547861
4FGLJ1410.7+7405	XRTJ141045.6+740509.8	JVLAJ141046.00+740511.2*	PANJ141045.95+740510.8	212.691458	74.086333
4FGLJ1430.6+1543	XRTJ143057.9+154555.0	-	SDSSJ143058.03+154555.6	217.741792	15.765444
4FGLJ1535.9+3743	XRTJ153550.56+374056.8	VLASS1QLCIR J153550.56+374055.5	SDSSJ153550.54+374055.6	233.960583	37.682111
4FGLJ1539.1+1008	XRTJ153848.5+101841.7	-	SDSSJ153848.47+101843.2	234.701958	10.312000
4FGLJ1544.9+3218	XRTJ154433.1+322148.5	VLASS1QLCIRJ154433.20+322149.1	SDSSJ154433.19+322149.1	236.138292	32.363639
4FGLJ1554.2+2008	XRTJ155424.1+201125.3	VLASS1QLCIRJ155424.15+201125.5	SDSSJ155424.12+201125.4	238.600500	20.190389
4FGLJ1555.3+2903	XRTJ155513.0+290328.0	VLASS1QLCIRJ155512.89+290330.0	SDSSJ155512.91+290329.9	238.803792	29.058306
4FGLJ1631.8+4144	XRTJ163146.8+414631.8	VLASS1QLCIRJ163146.74+414632.7	SDSSJ163146.72+414632.8	247.944667	41.775778
4FGLJ1648.7+4834	XRTJ164900.5+483409.1	VLASS1QLCIRJ164900.35+483411.7	SDSSJ164900.34+483411.8	252.251417	48.569944
4FGLJ2030.0-0310	XRTJ203014.3-030722.8	ATCAJ203014.27-030721.8	PANJ203014.27-030722.56	307.559458	-3.122933
4FGLJ2207.1+2222	XRTJ220704.1+222231.8	VLASS1QLCIRJ220704.09+222231.5	SDSSJ220704.10+222231.4	331.767083	22.375389
4FGLJ2240.3-5241	XRTJ224017.55-524112.3	RACS224017.79-524111.1	DESJ224017.71-524113.7	340.073792	-52.687139
4FGLJ2317.7+2839	XRTJ231740.1+283955.4	VLASS1QLCIRJ231740.21+283955.8	SDSSJ231740.00+283955.7	349.416667	28.665472
4FGLJ2323.1+2040	XRTJ232320.30+203523.6	VLASS1QLCIRJ232319.95+203523.7	SDSSJ232320.34+203523.4	350.834772	20.589860
4FGLJ2353.2+3135	XRTJ235319.39+313616.9	VLASS1QLCIRJ235319.50+313616.8	SDSSJ235319.54+313616.7	358.331417	31.604639

**Note.** Column 1: 4FGL Name of the target; Column 2: X-ray counterpart; Column 3: Radio counterpart (Names report the acronym of the radio facility plus the J2000 sexagesimal coordinates); Column 4: Optical counterpart; Column 5-6: Coordinates of the optical counterpart in degrees.

(\*) Radio source proposed by (Marchesini et al. 2023)

jects with redshift  $z < 0.5$ , all galaxies are resolved, except for 4FGLJ0112.0+3442, and the results are reported in Table 4.

The optical properties and the multiwavelength emission data of the 33 UGS are summarized in Tab. 5. While  $\gamma$ -ray, optical and radio fluxes come from catalogs, the X-ray fluxes are extracted through spectral fits. Spectra are fitted using an absorbed power-law, where the NH parameter, defined as the equivalent hydrogen column (in units of  $10^{22}$  atoms  $\text{cm}^{-2}$ ), was set to the equivalent Galactic value in the direction of the source (HI4PI Collaboration et al. 2016). Fluxes are estimated in the energy range 0.3 - 10 keV. For each source, we evaluate a *radio-loudness* parameter  $R$  defined as the ratio between the radio flux (in the range 2 - 4 GHz) and the optical band flux of the nucleus component (see Table 5). We consider a source as radio loud if  $R > 10$  (Kellermann et al. 1989). All BLL are radio loud sources.

About the other 12 sources, 4 sources (4FGLJ0023.6-4209, 4FGLJ0938.8+5155, 4FGLJ1346.5+5330 and 4FGLJ1535.9+3743) can be classified as radio-loud, two have  $R < 10$ , and six are not detected in the radio images, allowing us to put an upper limit on  $R$ .

Based on the absolute magnitude ( $M_{\text{abs}} < -23$  for QSO, e.g. Osterbrock 1980) and the optical imaging analysis (see details in Section 2.1.3), four sources have the typical luminosity of the QSO:

4FGLJ1535.9+3743 is a radio-loud quasar and 4FGLJ1125.1+4811, 4FGLJ1256.8+5329 and 4FGLJ1308.7+0347 radio quiet quasars. The other eight objects can be classified as Seyfert galaxies.

## 4 SUMMARY AND CONCLUSIONS

We have examined a set of 33 UGS counterparts for which an optical spectrum was recovered in the literature. From the spectroscopic analysis we found that all counterparts are extragalactic objects: 21 sources have been classified as BLL, while the others 12 are AGN with prominent emission lines.

In particular we found that among the 21 BLL, 7 are notable for having their redshift determined solely through the detection of absorption lines due to the host galaxy, while one object (4FGLJ0112.0+3442) exhibits both absorption and emission lines. For two BLLs, spectroscopic redshift lower limit can be set on the based of the detection of intervening absorption lines. The others have a featureless spectrum, described by a power-law shape, and the redshift is unknown.

The average  $\gamma$ -ray luminosity of the BLL in the sample

**Table 3.** Optical properties of the 33 UGSs with only one X-ray counterpart within the  $3\sigma$  Fermi error box

4FGL Name	Optical counterpart	g	r	Spectrum Reference	Line type	Redshift	Spectrum Class
4FGLJ0023.6-4209	DESJ002303.74-420508.4	15.6	15.0	6dF	e	0.053	Type-2
4FGLJ0112.0+3442	SDSSJ011124.86+344154.6	19.4	19.0	SDSS	e,g	0.3997	BLL
4FGLJ0117.9+1430	SDSSJ011804.83+143158.6	18.7	18.3	SDSS	e	0.129	Type-1
4FGLJ0202.7+3133	SDSSJ020242.06+313210.9	18.7	18.4	SDSS	-	? *	BLL
4FGLJ0251.1-1830	PANJ025111.53-183112.7	20.2	19.6	Paiano et al. (2019)	i	>0.615	BLL
4FGLJ0259.0+0552	SDSSJ025857.55+055243.9	18.6	18.3	Paiano et al. (2019)	-	?	BLL
4FGLJ0641.4+3349	PANJ064111.22+334459.7	17.1	16.4	Monroe et al. (2016)	e	0.1657	Type-1
4FGLJ0838.5+4013	SDSSJ083903.08+401545.6	18.2	17.0	SDSS	g	0.1945	BLG
4FGLJ0938.8+5155	SDSSJ093834.72+515452.3	20.3	20.1	SDSS	e	0.4168	Type-1
4FGLJ1016.1-4247	USNOJ101620.67-424722.6	19.3	18.2	Rajagopal et al. (2023)	-	?	BLL
4FGLJ1039.2+3258	SDSSJ103852.17+325651.6	19.7	18.9	SDSS	-	? *	BLL
4FGLJ1049.8+2741	SDSSJ104938.79+274213.0	18.2	17.3	SDSS, de Menezes et al. (2019)	g	0.144	BLG
4FGLJ1125.1+4811	SDSSJ112526.27+480922.0	20.3	20.2	SDSS	e	1.649	Type-1
4FGLJ1131.6+4657	SDSSJ113142.27+470008.6	17.5	16.5	SDSS	g	0.1255	BLG
4FGLJ1146.0-0638	USNOB1-0833-0250645	19.5	19.7	Paiano et al. (2019)	g	0.6407	BLL
4FGLJ1256.8+5329	SDSSJ125630.43+533204.3	20.6	20.3	SDSS	e	0.996	Type-1
4FGLJ1308.7+0347	SDSSJ130832.10+034403.9	17.2	17.3	SDSS	e	0.6193	Type-1
4FGLJ1346.5+5330	SDSSJ134545.36+533252.3	17.0	16.6	SDSS	e	0.1359	Type-1
4FGLJ1410.7+7405	PANJ141045.95+740510.8	19.2	19.3	Marchesini et al. (2023)	-	?	BLL
4FGLJ1430.6+1543	SDSSJ143058.03+154555.6	17.4	16.9	SDSS	e	0.1633	Type-1
4FGLJ1535.9+3743	SDSSJ153550.54+374055.6	19.7	19.4	SDSS	e	0.6255	Type-1
4FGLJ1539.1+1008	SDSSJ153848.47+101843.2	18.3	18.0	SDSS	e	0.2345	Type-1
4FGLJ1544.9+3218	SDSSJ154433.19+322149.1	18.7	18.4	SDSS	-	? *	BLL
4FGLJ1554.2+2008	SDSSJ155424.12+201125.4	18.1	17.2	SDSS	g	0.2225	BLG
4FGLJ1555.3+2903	SDSSJ155512.91+290329.9	18.2	17.2	SDSS	g	0.1767	BLG
4FGLJ1631.8+4144	SDSSJ163146.72+414632.8	20.5	20.4	SDSS	-	? *	BLL
4FGLJ1648.7+4834	SDSSJ164900.34+483411.8	19.4	19.1	SDSS	-	? *	BLL
4FGLJ2030.0-0310	PANJ203014.27-030722.56	16.8	16.2	6dF	e	0.036	Type-2
4FGLJ2207.1+2222	SDSSJ220704.10+222231.4	20.4	19.9	SDSS	-	? *	BLL
4FGLJ2240.3-5241	DESJ224017.71-524113.7	18.1	17.4	Desai et al. (2019)	-	?	BLL
4FGLJ2317.7+2839	SDSSJ231740.00+283955.7	19.6	19.1	SDSS	-	? *	BLL
4FGLJ2323.1+2040	SDSSJ232320.34+203523.4	14.4	13.4	Marcha et al. (1996)	g	0.038	BLG
4FGLJ2353.2+3135	SDSSJ235319.54+313616.7	20.5	20.5	SDSS	i	>0.8809*	BLL

**Note.** Column 1: 4FGL Name of the target; Column 2: Optical counterpart; Column 3-4: magnitude in g and r band from PANSTARRs; Column 5: Reference of the optical spectrum; Column 6: Type of the detected lines: e = emission lines, g = absorption lines from the host galaxy, i = intervening absorption lines; Column 7: Redshift; Column 8: Classification based on the optical spectrum.

(\* ) New redshift estimates reported for the first time by this work. It is worth noting that, for a given number of sources, the literature redshift was disproved and then they are not known (except in one case, where we determined a lower limit). Details are reported in Sec. 5

( $\langle L_\gamma \rangle = 10^{44}$  erg s $^{-1}$ ), is found significantly lower than that ( $\langle L_\gamma \rangle > \sim 10^{45}$  erg s $^{-1}$ ) of  $\sim 900$  BLL of the 4FGL-DR3 catalog (see also Table 6). While, regarding radio band, all BLL are radio-loud sources. It is worth noting that 4FGLJ1410.7+7405 identified as a candidate Radio Weak BL Lac (RWBL) by Marchesini et al. (2023) and Massaro et al. (2017), turns out to instead be a radio loud BLL using the radio flux value estimated in the same work by Marchesini et al. (2023). From the imaging decomposition (see Table 4), the absolute magnitude of their host galaxies in the optical r-band is in the range  $-23.1 < M(r) < -21.2$ , with  $\langle M(r) \rangle = -22.4$ . These values are consistent with that typical of BLL host galaxies  $\langle M(r) \rangle = -22.9$  (Urry et al. 2000; Sbarufatti et al. 2005). The indication is therefore that these UGSs identified as BLL belong to the same population of already identified Fermi BLL, covering the faint tail of this luminosity Fermi BLL distribution (see Table 6).

The other 12 UGS of this study are characterized by optical spectra with strong emission lines and constitute  $\sim 40\%$  of the total of our studied sources. This fraction is in fact in agreement with the larger statistics of the Fourth Catalog of Active Galactic Nuclei detected by Fermi - Data Release 3 (4LAC-DR3, Ajello et al. 2020, 2022) ( $\sim 1400$  BLL and  $\sim 800$  FSRQ) and it is much greater than  $\sim 10\%$

found in our earlier studies of UGS (Paiano et al. 2017d, 2019) for which only 3 objects showed a spectrum not compatible with a BLL classification. Note that they were based on the 2FGL and 3FGL catalogues (Nolan et al. 2012; Acero et al. 2015) which explored fluxes sensibly higher than those examined here (see Table 6).

More specifically, we found one radio-loud quasar (4FGLJ1535.9+3743), three radio-quiet quasars (4FGLJ1125.1+4811, 4FGLJ1256.8+5329 and 4FGLJ1308.7+0347) and eight Seyfert-like objects. 4FGLJ0023.6-4209 and 4FGLJ2030.0-0310, two Type-2 AGN, are the closest sources of the sample with  $z \leq 0.05$  and have the smallest  $\gamma$ -ray luminosity (see Table 5). 4FGLJ0117.9+1430 is classified as a NLSy1 (see the note of the source in Section 5). This increases the total number of objects classified as Seyfert of the 4FGL-DR3 catalog (8 NLSy and 3 Seyfert).

It is of interest to compare the values of the radio-loudness ( $R$ ) found in our sample of 33 objects with the results of 4LAC, which are summarized in the distribution reported in Fig. 3. It is apparent that our 21 BLL have  $R$  indexes which are in the low part of the distribution. The median value is  $R=120$  to be compared with that  $R=230$  for the 4LAC BLL. We also compared the distribution of

**Table 4.** Results of the analysis and decomposition of the PANSTARRs images

4FGL Name	$z$	$r$	$r_n$	$r_h$	$M(r)_h$	$R_e$	$n$	N/H
4FGLJ0023.6-4209*	0.053	14.9	>18.5	14.9	-21.9	6.8	1.4	<0.05
4FGLJ0112.0+3442	0.3997	18.7	19.0	20.4	>-21.3	7*	4	4
4FGLJ0117.9+1430	0.129	18.2	19.4	18.5	-20.4	2.0	4	0.4
4FGLJ0641.4+3349	0.1657	16.3	17.1	16.7	-22.8	7*	5	0.7
4FGLJ0838.5+4013	0.1945	16.9	19.1	16.7	-23.1	10.5	4	0.1
4FGLJ0938.8+5155	0.4168	19.8	20.4	20.6	-21.2	10.7	4	1
4FGLJ1049.8+2741	0.144	17.2	19.0	17.2	-21.9	5.1	4	0.25
4FGLJ1131.6+4657	0.1255	16.4	18.9	16.3	-22.5	7.6	4	0.1
4FGLJ1346.5+5330	0.1359	16.4	17.8	16.7	-22.3	4	4	0.4
4FGLJ1430.6+1543	0.1633	16.8	18.0	17.1	-22.3	5.9	2.1	0.4
4FGLJ1539.1+1008	0.2345	17.9	18.3	19.2	-21.1	3.6	3.0	2.5
4FGLJ1554.2+2008	0.2225	16.9	18.3	17.2	-23.0	7.9	4	0.4
4FGLJ1555.3+2903	0.1767	17.0	19.3	17.0	-22.6	7.3	4	0.1
4FGLJ2030.0-0310	0.036	16.1	18.8	16.1	-19.8	1.1	1.9	0.1
4FGLJ2323.1+2040*	0.038	13.6	>17.0	13.6	-22.5	6.5	4	<0.05

**Note.** Column 1: Fermi name, Column 2: Redshift, Column 3:  $r$  from aperture photometry of the PANSTARRs image, Column 4-5: apparent magnitude of the nucleus ( $r_n$ ) and of the host galaxy ( $r_h$ ) derived by the imaging analysis, Column 6: Absolute magnitude of the host galaxy, Column 7: Effective radius (kpc), Column 8: Sersic index  $n$ , Column 9: Galaxy flux to nucleus flux ratio.

(\*) For 4FGLJ0023.6-4209 the DES image is used and for 4FGLJ2323.1+2040 we used the SDSS image.

R values of the 12 objects with prominent emission lines with the 4LAC FSRQ one. We found a significant difference and, as expected for the case of Seyfert galaxies, their *radio-loudness* value is well below the 4LAC FSRQ one (median  $R=5600$ ; see Figure 3).

The presence of a sizeable fraction of radio faint objects, in particular  $\geq 5$  sources have  $R$  smaller than 10, among the UGS counterparts is somewhat unexpected but not implausible (Massaro et al. 2017; Järvelä, Berton, & Crepaldi 2021). The obvious comment is that our current search for UGS counterparts is completely independent of the radio brightness, which is gathered *a posteriori*, it rather depends on the choice of the significance of the X-ray detection. In spite of the rather small sample the issue of radio quiet counterparts of  $\gamma$ -ray sources is of potentially great interest since they may represent a poorly explored type of  $\gamma$ -ray objects.

## 5 NOTES ON INDIVIDUAL SOURCES

4FGLJ0023.6-4209 - DESJ002303.74-420508.4: In the Swift/XRT image we find the source XRTJ002303.5-420509.6 as the likely X-ray counterpart for this UGS. It coincides with the optical source DESJ002303.74-420508.4 ( $g=15.6$ ), and the radio source J002303.61-420509.57, detected from the analysis of radio RACS data covering the UGS sky region (see Fig. B2). The radio source appears point-like and it has a density flux  $F = 3.3$  mJy that corresponds to a radio-loudness  $R > 15$  (see Tables 4 and 5). In the uncalibrated 6dF Galaxy Redshift survey optical spectrum, we are able to detect prominent and narrow emission lines attributed to  $H_\beta$  4861, [O III] 4959,5007,  $H_\alpha$  6563, [N II] 6583 and [S II] 6717,6731 at  $z = 0.053$ . No broad lines are found. The emission line properties of this object are typical of Seyfert 2 galaxies and from a inspection of the optical image (see Fig. B2) the host galaxy appears as spiral galaxy. Given the remarkably proximity ( $z < 0.053$ ), the  $\gamma$ -ray luminosity of 4FGLJ0023.6-4209 is  $\sim 10^{43}$  erg/s, one of the weakest of our sample.

4FGLJ0112.0+3442 - SDSSJ01124.86+344154.6: From the Swift/XRT analysis, we reveal the X-ray source XRTJ01124.8+344154.1 within the Fermi error box. The

sources is positionally coincident with the radio source VLASS1QLCIRJ01124.83+344154.5 and the optical source SDSSJ01124.86+344154.6. The optical spectrum, available in the SDSS archive, shows [O II] and [O III] emission lines and the Ca II doublet absorption lines consistent with redshift  $z=0.3397$ . Given the power-law shape of the spectrum, the source can be classified as a BLL. It is worth to note that this UGS is one of three sources listed in the 4FGL that lies within the event radius of the neutrino event IceCube-230511A<sup>8</sup>.

4FGLJ0117.9+1430 - SDSSJ011804.83+143158.6: Within the Fermi error box of this UGS, we detect the X-ray source XRTJ011804.7+143159.5 coincident with the optical source SDSSJ011804.83+143158.6 ( $g = 18.7$ ). No radio counterpart is found in the NVSS and VLASS catalogue. From the RACS data we can estimate the radio flux upper limit of 4.2 mJy/beam (within  $5\sigma$ ). The SDSS spectrum clearly shows prominent emission lines ( $H_\delta$  4102,  $H_\gamma$  4340,  $H_\beta$  4861 and [O III] 4959,5007) at  $z = 0.129$ . We note that the Balmer lines show broad components and in particular, based on the  $H_\beta$  4861 width (FWHM  $\sim 500$  km/s) and on the line ratio ([OIII] 5007/ $H_\beta$ )  $\sim 1$  (see e.g. Komossa 2008), we can classify the source as a NLSy1, according to that reported by Rakshit et al. (2017).

4FGLJ0202.7+3133 - SDSSJ020242.06+313210.9: We propose the source XRTJ020242.13+313211.4, found in the Swift/XRT skymap, as the X-ray counterpart for this UGS, spatially coincident with the optical object SDSSJ020242.06+313210.9 ( $g = 18.7$ ) and the radio source VLASS1QLCIRJ020242.03+313211.0. The SDSS spectrum appears featureless and exhibits the characteristic power-law continuum of the BLL.

4FGLJ0641.4+3349 - PANJ064111.22+334459.7: From the Swift/XRT imaging analysis, in the 4FGL error box of this  $\gamma$ -ray emitter, we find the X-ray source XRTJ064111.24+334502.0, coincident with the radio source VLASS1QLCIRJ064111.20+334459.6 (1.2 mJy) and the optical source PANJ064111.22+334459.7

<sup>8</sup> <https://gcn.nasa.gov/circulars/33773?page=5>

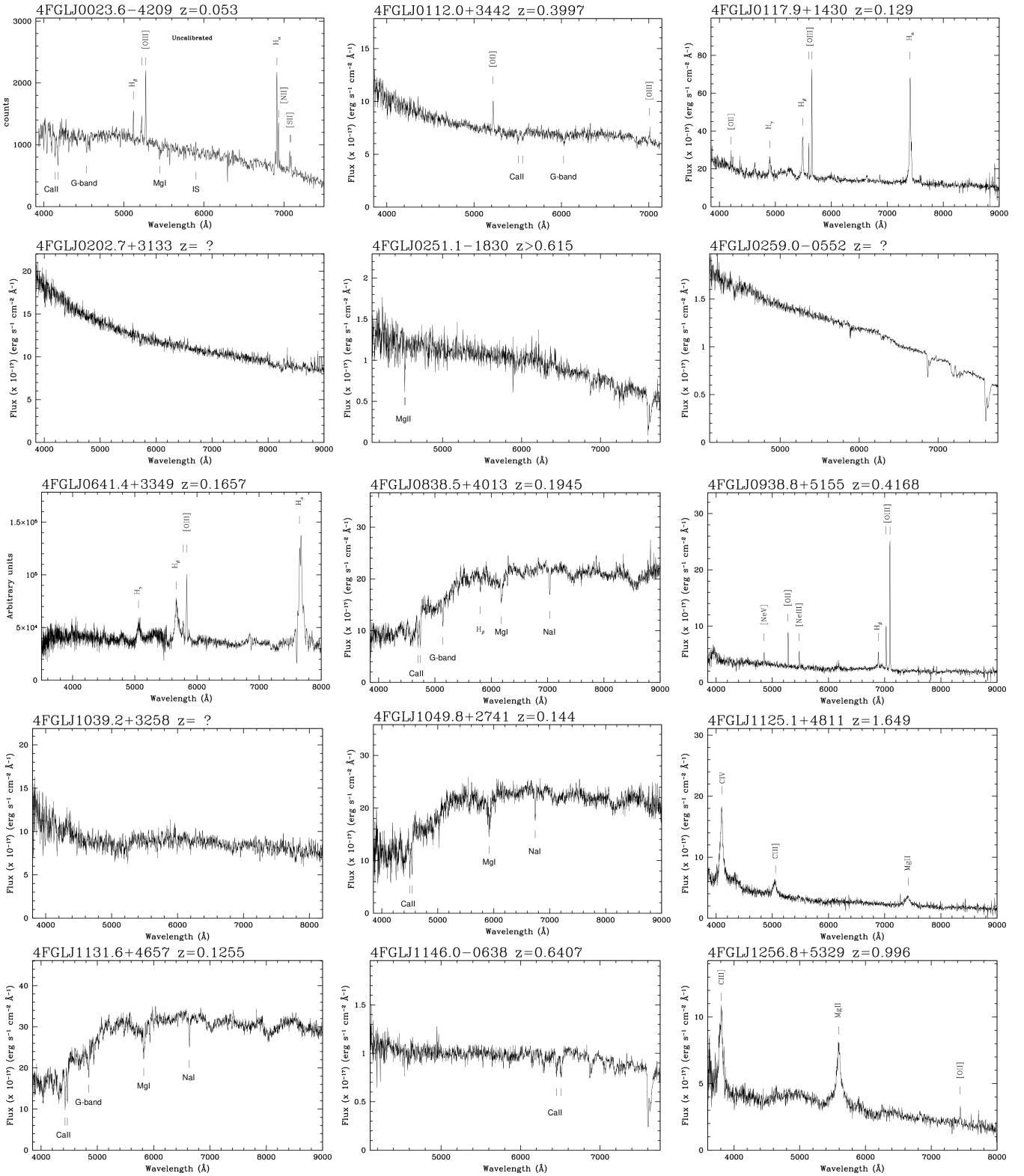


**Figure 2.** Optical spectra of the counterparts of UGS with only one X-ray detection within the  $3\sigma$  Fermi error ellipses (see text and Table 2 and 3 for details).



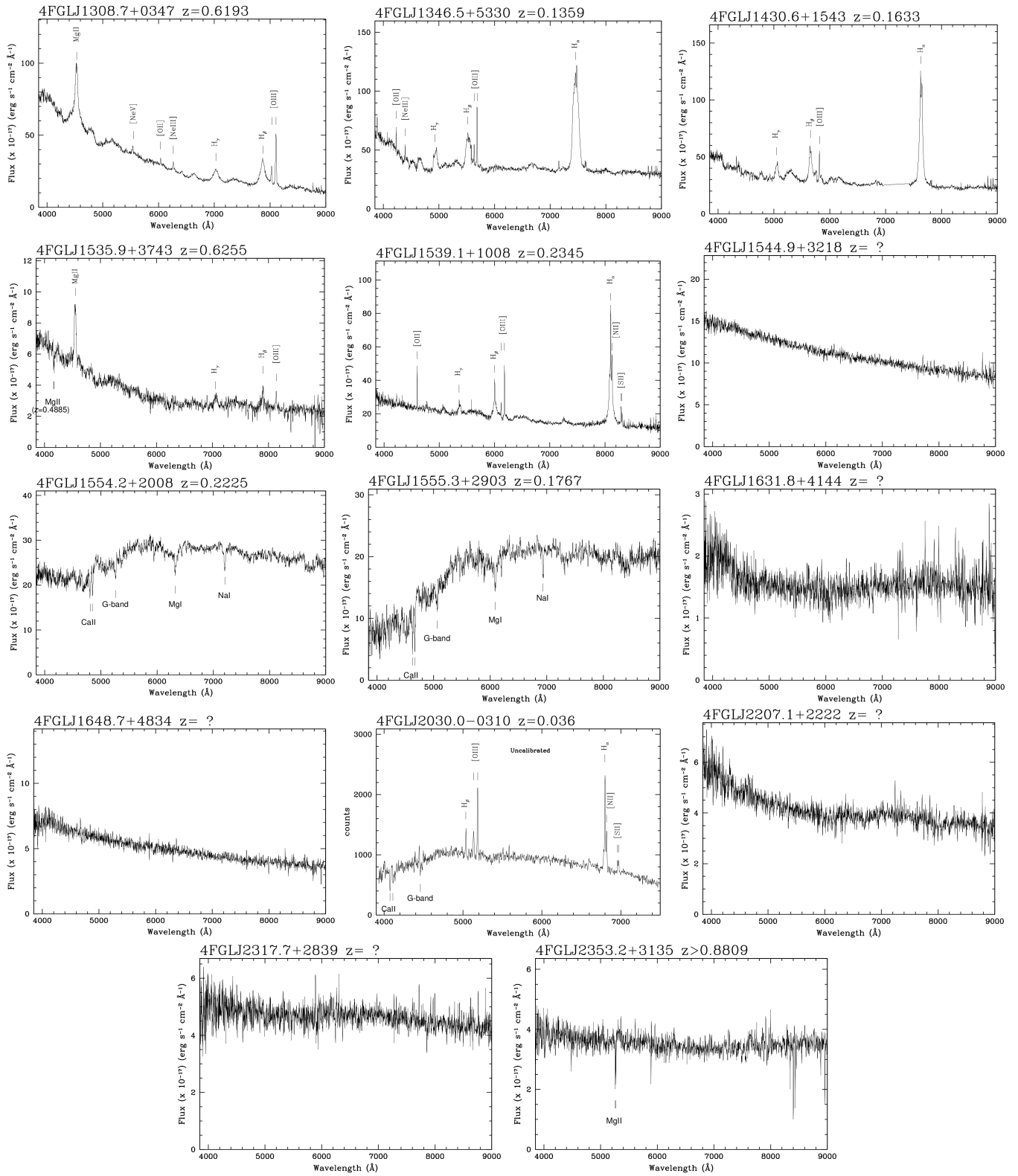


Figure 2. Continued.

**Table 5.** Multiwavelength fluxes and luminosities of the lower energy counterparts of the 33 UGSs

4FGL Name	$F_\gamma$	$f_v^{\text{radio}}$	$F_X$	$f_v^{\text{opt}}$	$L_\gamma$	$L_{\text{radio}}$	$L_X$	$M_g (M_r)$	$R$
BLL and BLG	$[\times 10^{-12}]$		$[\times 10^{-13}]$	$[\times 10^{-28}]$	$[\times 10^{45}]$	$[\times 10^{40}]$	$[\times 10^{44}]$		
4FGLJ0112.0+3442	1.4	41	2.5	6.3	0.9	74	1.5	-22.3 (-22.7)	450
4FGLJ0202.7+3133	1.0	15	3.8	12	-	-	-	-	125
4FGLJ0251.1-1830	1.8	8.8	5.5	3.3	-	-	-	-	265
4FGLJ0259.0+0552	6.8	5.8	4.1	13	-	-	-	-	45
4FGLJ0838.5+4013	0.9	24	4.6	19	0.1	8.3	0.5	-21.7 (-22.9)	290
4FGLJ1016.1-4247	3.1	7.2	5.8	6.9	-	-	-	-	100
4FGLJ1039.2+3258	2.7	6.1	2.9	4.8	-	-	-	-	130
4FGLJ1049.8+2741	1.4	7.2	2.9	19	0.1	1.3	0.2	-21.0 (-21.9)	80
4FGLJ1131.6+4657	1.1	92	4.5	36	0.1	1.2	0.2	-21.3 (-22.3)	920
4FGLJ1146.0-0638	3.1	5.8	5.4	5.8	5.7	32	10	-23.4 (-23.2)	100
4FGLJ1410.7+7405	3.6	2.4	1.1	7.6	-	-	-	-	30
4FGLJ1544.9+3218	1.4	12	3.6	12	-	-	-	-	100
4FGLJ1554.2+2008	2.7	42	6.1	21	0.4	20	10	-22.1 (-23.0)	240
4FGLJ1555.3+2903	1.1	22	3.2	19	0.1	6.1	0.3	-21.5 (-22.5)	320
4FGLJ1631.8+4144	1.3	0.8	8.1	2.3	-	-	-	-	35
4FGLJ1648.7+4834	1.2	2.5	6.0	6.3	-	-	-	-	40
4FGLJ2207.1+2222	1.7	6.5	2.6	2.5	-	-	-	-	260
4FGLJ2240.3-5241	6.2	29	1.9	21	-	-	-	-	135
4FGLJ2317.7+2839	2.8	4.5	0.8	5.2	-	-	-	-	90
4FGLJ2323.1+2040	2.4	2.4	4.9	631.0	0.01	0.03	0.02	-21.9 (-23.0)	>5
4FGLJ2353.2+3135	3.6	61	1.5	2.3	-	-	-	-	2650
Objects with prominent lines									
4FGLJ0023.6-4209	1.1	3.3	12	209	0.01	0.02	0.08	-21.3 (-21.9)	>15
4FGLJ0117.9+1430	2.9	<4.2	4.9	12	0.1	<0.03	0.2	-20.2 (-20.6)	<65
4FGLJ0641.4+3349	1.3	1.2	28	53	0.1	0.3	2.3	-22.4 (-23.1)	2.5
4FGLJ0938.8+5155	1.2	0.6	0.7	2.8	0.8	0.06	0.5	-21.5 (-21.7)	25
4FGLJ1125.1+4811	0.8	<0.6	0.4	2.8	14.5	<1.5	7.0	-25.1 (-25.2)	<20
4FGLJ1256.8+5329	2.7	<1.6	1.7	2.1	14.7	<1.3	9.1	-23.5 (-23.8)	<75
4FGLJ1308.7+0347	2.0	<0.2	7.5	48	3.3	<1.0	13	-25.6 (-25.5)	<0.5
4FGLJ1346.5+5330	3.0	250	44	58	0.2	39	2.3	-22.0 (-22.4)	900
4FGLJ1430.6+1543	0.9	<1.0	14	40	0.1	<0.2	1.1	-22.1 (-22.6)	<4.5
4FGLJ1535.9+3743	4.9	26	1.1	4.8	8.5	6.6	2.0	-23.2 (-23.5)	540
4FGLJ1539.1+1008	2.2	<1.0	3.1	17	0.4	<0.5	0.5	-22.0 (-22.3)	<6.0
4FGLJ2030.0-0310	0.7	0.4	11	69	0.002	<0.03	0.03	-19.2 (-19.8)	3.5

**Note.** Column 1: 4FGL Name of the target; Column 2:  $\gamma$ -ray flux ( $\text{erg cm}^{-2} \text{s}^{-1}$ ) in the 100 MeV to 100 GeV range; Column 3: Radio density flux (mJy); Column 4: X-ray flux ( $\text{erg cm}^{-2} \text{s}^{-1}$ ) in the 0.3-10 keV range; Column 5: Optical density flux ( $\text{erg cm}^{-2} \text{s}^{-1} \text{Hz}^{-1}$ ); Column 6-7-8:  $\gamma$ -ray, radio and X-ray luminosity ( $\text{erg s}^{-1}$ ); Column 9: g-band and r-band absolute magnitude of the target (derived from PANSTARRs images); Column 10: *radio-loudness* define as the ratio between radio flux density and optical flux density of the nuclear component.

**Table 6.** Statistics on Redshift, Flux and Luminosity; Comparison of UFO3 with UFO 1+2 and 4FGL-DR3 catalog

Sample	$\langle z \rangle$	$F_\gamma (\text{erg cm}^{-2} \text{s}^{-1}) \times 10^{-12}$	$L_\gamma (\text{erg s}^{-1}) \times 10^{45}$
8 BLL/BLG of this work	0.2	$1.4 \pm 0.4$	$0.1 \pm 0.1$
12 QSO/Seyfert-like of this work	0.2	$1.3 \pm 0.7$	$0.3 \pm 0.3$
875 BLL of 4LAC	0.3	$3.1 \pm 1.7$	$1.2 \pm 1.1$
792 FSRQ of 4LAC	1.1	$5.5 \pm 3.4$	$45 \pm 40$
24 BLL-UGS of Paiano et al 2017,2019	0.4	$2.9 \pm 1.0$	$2.0 \pm 1.3$
3 QSO/Sy-like UGS of Paiano et al 2017,2019	0.3	$4.7 \pm 1.4$	$0.6 \pm 0.1$

**Note.** Column 1: Sample under investigation; Column 2: Median redshift; Column 3: Median energy flux from 4FGL catalog in the 100 MeV to 100 GeV range; Column 4: median luminosity. The reported uncertainty indicates the rms of the distribution.

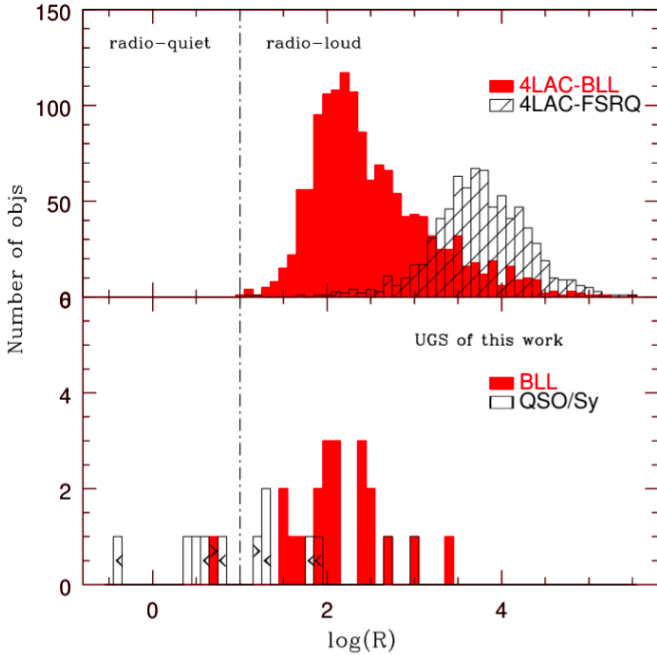


**Figure 3.** *Upper panel:* Distribution of the *radio-loudness* parameter ( $\log(R)$ ) value for 1409 objects classified as BLL and 771 objects as FSRQ of the 4LAC catalog. *Bottom panel:* Distribution of the *radio-loudness* value for the counterparts of the 33 UGS of this work. The black dashed vertical line represent the *radio-loudness* parameter value ( $R = 10$ ) that separates the radio-quiet from the radio-loud sources.

( $g=17.1$ ). The spectrum of the optical source, available in [Monroe et al. \(2016\)](#), shows prominent narrow emission lines due [OIII] 4959,5007 and broad  $H_\gamma$  4340,  $H_\beta$  4861 and  $H_\alpha$  6564 emission lines at redshift  $z=0.1657$ . On the basis of the absolute magnitude, the radio-loudness  $R \sim 2.5$  and the emission lines properties, this object can be classified as a low redshift radio quiet QSO.

4FGLJ0838.5+4013 - SDSSJ083903.08+401545.6: Inside the *Fermi* error box of this UGS we find the X-ray source XRTJ083902.9+401546.9 coincident with the radio source VLASS1QLCIRJ083903.07+401545.6 ([Joffre et al. 2022](#)) and the optical source SDSSJ083903.08+401545.6. [Kaur, Kerby, & Falcone \(2023\)](#) and [Joffre et al. \(2022\)](#) through a machine learning analysis proposed the X-ray object as a BLL candidate. The SDSS spectrum is dominated by a galactic component and we can identify several absorption lines (Ca II, G-band, Mg I, and Na II) at  $z = 0.1945$  due to old stellar population of the host galaxy. The source can be classify as a galaxy-dominated BLL in agreement with what reported in the BZCAT catalog.

4FGLJ0938.8+5155 - SDSSJ093834.72+515452.3: Through the inspection of *Swift*/XRT data, we find the X-ray source XRTJ093834.5+515454.7 inside the  $3\sigma$  *Fermi* error ellipse. Analysing radio data of the LoTSS survey we found a radio detection J093834.68+515451.8 (0.6mJy) coincident with the X-ray source. A SDSS spectrum available for the optical counterpart SDSSJ093834.72+515452.3 ( $g=20.3$ ) shows prominent and narrow emission lines attributed to [O II],  $H_\gamma$ ,  $H_\beta$ , [O III],  $H_\alpha$  and [N II] consistent with  $z=0.4168$ . A broad component is present for the  $H_\beta$  and  $H_\alpha$ . Based on this information, the target can be classified as a

radio loud QSO.

4FGLJ1039.2+3258 - SDSSJ103852.17+325651.6: We propose the X-ray source XRTJ103852.1+325651.9 found inside the *Fermi* error box of this  $\gamma$ -ray emitter as the likely lower energy counterpart. It is coincident with the radio source VLASS1QLCIRJ103852.17+325651.9 and the optical source SDSSJ103852.17+325651.6. The modest quality SDSS spectrum, reported also in [de Menezes et al. \(2019\)](#) and associated to the IR source WISEJ103852.20+325651.7, appears featureless typical of BLL, although a possible weak signature of CaII break at  $\sim 5200$  can be recognized yielding a tentative redshift of 0.32.

4FGLJ1049.8+2741 - SDSSJ104938.79+274213.0: Inside the 4FGL sky region of this UGS we find the X-ray source XRTJ104938.7+274212.0, that spatially coincides with the the radio source VLASS1QLCIRJ104938.81+274213.1 and the optical source SDSSJ104938.79+274213.0 ( $g=18.2$ ). The optical spectrum provided by the SDSS survey is dominated by the component of the elliptical host galaxy ( $N/H=0.25$  see Table 4) and a number of relevant absorption features are present: the CaII doublet, G-band, MgI and NaI at  $z=0.144$ .

4FGLJ1125.1+4811 - SDSSJ112526.27+480922.0: We find the X-ray source XRTJ112526.0+480922.8 inside the  $\gamma$ -ray  $3\sigma$  error ellipse of this UGS. It is spatially coincident with the optical source SDSSJ112526.27+480922.0 ( $g=20.3$ ). From the analysis of LOTSS radio data, no radio counterpart is found, in agreement with [Gürkan et al. \(2019\)](#). In the optical spectrum, obtained by the SDSS survey, we can detect broad emission lines attributed to CIV, C III and Mg II consistent with  $z=1.649$ . On the basis of this spectrum and of the MWL information, we can classify this source as a radio-quiet QSO. Within  $4\sigma$  *Fermi* error box of this  $\gamma$ -ray emitter, another X-ray source is present, XRTJ112432.5+480741.0, coincident with the radio source VLASS1QLCIRJ112432.64+480739.9 and the optical source SDSSJ112432.65+480740.7 ( $g=22.7$ ). An optical spectrum is available in the SDSS archive for this source. The power-law trend of the spectrum, absent of emission or absorption lines, indicates that the object is a BLL.

4FGLJ1131.6+4657 - SDSSJ113142.27+470008.6: The *Swift*/XRT analysis reveals the source XRTJ113142.3+470009.2 as X-ray counterpart of this UGS. The radio source VLASS1QLCIRJ113142.36+470009.4 and the optical source SDSSJ113142.27+470008.6 are coincident with the X-ray emission. The SDSS survey provides the optical spectrum with absorption lines (Ca II, G-band, MgI, Ca+Fe and NaI) due to the old stellar population of the elliptical host galaxy. The spectral lines are consistent with a redshift  $z = 0.1255$  and the source can be classify as a galaxy-dominated BLL.

4FGLJ1256.8+5329 - SDSSJ125630.43+533204.3: The analysis of *Swift*/XRT data reveals only the X-ray source XRTJ125630.5+533202.2 within the *Fermi* error box of this  $\gamma$ -ray emitter. It is coincident with the optical source SDSSJ125630.43+533204.3. The optical spectrum exhibits broad emission lines due to CIII] and MgII at  $z=0.996$ . Also the narrow (EW=11.1) emission line due to [O II] at 7439 Å is present. We can classify the source as a QSO. From radio catalogs and the analysis of LoTSS data, no radio emission is coincident with the X-ray/optical counterpart.

4FGLJ1308.7+0347 - SDSSJ130832.10+034403.9: For this UGS, we find the X-ray source XRTJ130832.2+034405.3 slightly out of the *Fermi* error ellipse reported in the 4FGL-DR3, but inside the  $3\sigma$  error box (see Sec. 2). From the analysis of the SDSS optical spectrum we can detect prominent broad emission lines attributed to Mg II, H $\gamma$ , H $\beta$  and the doublet of narrow lines due to [O III]. The redshift of the source is  $z=0.6193$ . From our analysis of RACS radio data and from that reported by [Rusinek-Abarca & Sikora \(2021\)](#) using LoTSS data, no radio object is detected coincident with the optical counterpart that can be classified as a radio quiet QSO.

4FGLJ1346.5+5330 - SDSSJ134545.36+533252.3: The X-ray counterpart for this UGS, found by our Swift/XRT analysis, is XRTJ134545.1+533252.4. It coincides with the radio source VLASS1QLCIRJ134545.34+533252.1 and in the optical with SDSSJ134545.36+533252.3. The SDSS optical spectrum is a Seyfert 1-like (as also proposed by [Wang, Wang, & Dong 2009](#)) and exhibits several emission lines: narrow emission lines due to [OII], [OIII] and [OI] and the emission lines attributed to H $\delta$ , H $\gamma$ , H $\beta$  and H $\alpha$  that show a very prominent broad emission component. These lines set the source at  $z=0.1359$ . From the radio analysis of LOFAR Two Metre Sky Survey data, [Pajdosz-Śmierciak, Śmierciak, & Jamroz \(2022\)](#) show that the source exhibits a structure composed of a compact radio core, two-sided S-shaped jets and the radio luminosity characteristic of FR I radio galaxies.

4FGLJ1430.6+1543 - SDSSJ143058.03+154555.6: In the Swift/XRT skymap and within the *Fermi* error box of this  $\gamma$ -ray emitter we find the X-ray source XRTJ143057.9+154555.0 coincident with the optical source SDSSJ143058.03+154555.6. The optical spectrum, available in the SDSS archive, shows prominent and broad emission lines such as H $\gamma$ , H $\beta$ , H $\alpha$  together with the narrow lines due to the [O III] doublet at  $z=0.1633$  and consistent with a Seyfert-1 spectrum. In the radio band, no counterpart is detected ([Coziol et al. 2017](#)).

4FGLJ1535.9+3743 - SDSSJ153550.54+374055.6: Analysing the Swift/XRT data we find the X-ray source XRTJ153550.56+374056.8 inside the UGS *Fermi* error box. It is coincident with the radio source VLASS1QLCIRJ153550.56+374055.5 (26 mJy) and the optical source SDSSJ153550.54+374055.6 for which the spectrum is available. The spectrum shows a prominent emission line at 4551Å due to MgII, a weak and broad emission line attributed to H $\beta$  and the faint and narrow line of [OIII]. The redshift is  $z=0.6255$ . We note that also an intervening MgII absorption line is detected at  $\sim 4167$  ( $z=0.4885$ ). On the basis of the radio-loudness parameter ( $R\sim 550$ ) and the absolute optical magnitude ( $M_g = -23.2$ ) the source appears to be a radio loud quasar.

4FGLJ1539.1+1008 - SDSSJ153848.47+101843.2: From the Swift/XRT image, we find that the source XRTJ153848.5+101841.7 is a possible UGS X-ray counterpart. It is coincident with the optical source SDSSJ153848.47+101843.2. No radio emission is present ([Coziol et al. 2017](#)). The SDSS spectrum displays narrow lines due to [OII], [OIII] and [SII], H $\beta$  and H $\alpha$  emission lines with broad and narrow components. This can be classified as a Seyfert-1-like spectrum and sets the source at  $z=0.2345$ .

4FGLJ1544.9+3218 - SDSSJ154433.19+322149.1: From the analysis of Swift/XRT data, we propose the X-ray source XRTJ154433.1+322148.5, coincident with the radio source VLASS1QLCIRJ154433.20+322149.1 and the optical source

SDSSJ154433.19+322149.1, as lower energy counterpart of the  $\gamma$ -ray emitter. In the SDSS archive the optical spectrum is available showing the power-law shape and appearing featureless. We therefore classify the source as a BLL with unknown redshift.

4FGLJ1554.2+2008 - SDSSJ155424.12+201125.4: The optical source SDSSJ155424.12+201125.4 and the radio source VLASS1QLCIRJ155424.15+201125.5 are spatially coincident with the X-ray object XRTJ155424.1+201125.3 found inside the positional error box of this UGS and proposed as the likely counterpart. The optical spectrum of this source is provided by the SDSS survey and it is dominated by a galactic component with the presence of moderate non-thermal emission. Clear absorption features of the stellar population are detected, in particular Ca II 3934, 3968, G-band 4305, Mg I 5157, and NaI 5893 at  $z=0.2225$ . We classified the source as a BLG. It is also notably that the source is one of the possible counterparts of the neutrino event IceCube-110521A ([Giommi et al. 2020](#); [Padovani et al. 2022](#)).

4FGLJ1555.3+2903 - SDSSJ155512.91+290329.9: By the Swift/XRT data analysis, we found the X-ray source XRTJ155513.01+290328.0 inside the 4FGL-DR3 error box of this UGS, that coincides with the radio emitter VLASS1QLCIRJ155512.89+290330.0 and the optical source SDSSJ155512.91+290329.9. The SDSS spectrum is available and absorption lines due to Ca II doublet, G-band, Mg I and NaII are clearly detected at  $z=0.1747$ , allowing us to classify the source as a galaxy-dominated BLL.

4FGLJ1631.8+4144 - SDSSJ163146.72+414632.8: XRTJ163146.8+414631.8 is the only X-ray source detected inside the 4FGL-DR3 position error box and it is coincident with the radio source VLASS1QLCIRJ163146.74+414632.7 and the optical object SDSSJ163146.72+414632.8. In the SDSS spectrum the continuum is very flat and no emission lines are detected, allowing us to classify the source as a BLL. A possible CaII absorption doublet is present at  $\sim 6800$  Å yielding a tentative redshift of  $z=0.721$ .

4FGLJ1648.7+4834 - SDSSJ164900.34+483411.8: Through the Swift/XRT image analysis, we find the X-ray source XRTJ163146.8+414631.8 inside the positional error box of this UGS. We propose the spatially coincident objects VLASS1QLCIRJ163146.74+414632.7 and SDSSJ164900.34+483411.8 ( $g = 19.4$ ) as radio and optical counterparts. Our optical spectrum exhibits a featureless power-law continuum typical of BLL.

4FGLJ2030.0-0310 - PANJ203014.27-030722.56: The Swift/XRT image reveals the X-ray object XRTJ203014.3-030722.8 inside the 4FGL error box that is spatially coincident with the optical source PANJ203014.27-030722.56. RACS radio image reveals an hint of radio emission at the position of the X-ray source. As such, we observed 4FGLJ2030.0-0310 sky region with the Australia Telescope Compact Array (ATCA)<sup>9</sup>. We detected the source with

<sup>9</sup> The observations were carried out over two epochs, (2023-07-04 17:25:20 – 20:53:10 UT and 2023-07-05 13:07:30 – 20:49:30 UT). For both observations we used PKS 1934–638 for primary flux and bandpass calibration, and PKS 2044–027 for secondary gain calibration. Data were recorded at a central frequency of 2.1 GHz with 2 GHz of bandwidth composed of 2048 1-MHz channels. Raw data were then edited for radio frequency interference (RFI), calibrated, and imaged following standard procedures (details in <https://>

a SNR  $> 13 \sigma$  and we measured a radio flux density of  $0.40 \pm 0.03$  mJy at 2.1 GHz, corresponding to a radio-loudness  $R=3.5$  (see Table 4 and 5). The uncalibrated 6dF Galaxy Redshift survey optical spectrum shows prominent and narrow emission lines attributed to  $H_{\beta}$  4861, [O III] 4959,5007,  $H_{\alpha}$  6563, [N II] 6583 and [S II] 6717,6731 at  $z=0.036$ . No broad lines are found, therefore the spectrum can be classified as Type 2. Considering the very low redshift, the absolute optical magnitude ( $M_g = -19.2$ ) and the host galaxy properties from the analysis of the optical image (see Tab.4), the source should be classified as a Seyfert-2 galaxy hosted by a dwarf galaxy. It is important to mention that, given its remarkably close proximity ( $z < 0.036$ ), this object has a  $\gamma$ -ray luminosity of approximately  $2 \times 10^{42}$  erg/s, which is one of the lowest in our sample.

4FGLJ2207.1+2222 - SDSSJ220704.10+222231.4: The analysis of Swift-XRT imaging data reveals one X-ray object XRTJ220704.1+222231.8 in the 4FGL-DR3 error box that is spatially coincident with the optical source SDSSJ220704.10+222231.4 ( $g=20.4$ ) and the radio source VLASS1QLCIRJ220704.09+222231.5. The SDSS optical spectrum is characterized by a power-law emission and appears featureless typical of BLL. It is worth noting that this UGS is one of two sources listed in the 4FGL that lie within the event radius of the neutrino event IceCube-221210A<sup>10</sup>.

4FGLJ2317.7+2839 - SDSSJ231740.00+283955.7: Inside the *Fermi* error box of this UGS, we detected the X-ray source XRTJ231740.1+283955.4, coincident with the radio source VLASS1QLCIRJ231740.21+283955.8 and the optical source SDSSJ231740.00+283955.7. The optical spectrum, available in the SDSS archive, appears featureless with a power-law continuum. This source is therefore a BLL with redshift unknown.

4FGLJ2353.2+3135 - SDSSJ235319.54+313616.7: Through the *Swift*/XRT data analysis, we find that the X-ray source XRTJ235319.1+313613.4 is inside the 4FGL-DR3 position error box. The radio object VLASS1QLCIR J235319.50+313616.8 and the optical source SDSSJ235319.54+313616.7 are coincident with the X-ray emitter. The optical spectrum, available in the SDSS archive, is flat and characterized by a power-law continuum typical of BLL. It is clearly possible to detect an intervening absorption system due to MgII allowing us to set a redshift lower limit of  $z > 0.8809$ .

## ACKNOWLEDGMENTS

This work has been partially supported by the ASI-INAF program I/004/11/5 and made use of data supplied by the UK Swift Science Data Centre at the University of Leicester. This research uses services or data provided by the Astro Data Lab at NSF's National Optical-Infrared Astronomy Research Laboratory. NOIRLab is operated by the Association of Universities for Research in Astronomy (AURA), Inc. under a cooperative agreement with the National Science Foundation. We acknowledge the use of public data from the Swift data archive and we thank the Swift Observatory for scheduling and plan our proposed fill-in targets. Moreover we acknowledge

casaguides.nrao.edu/index.php/ATCA\_Tutorials) in the Common Astronomy Software Applications for radio astronomy (CASA, version 5.1.2; CASA Team et al. 2022)

<sup>10</sup> <https://gcn.nasa.gov/circulars/33040?page=12>

the use of data and software facilities from the SSDC, managed by the Italian Space Agency, and the United Nations 'Open Uni verse' initiative. Funding for SDSS-III has been provided by the Alfred P. Sloan Foundation, the Participating Institutions, the National Science Foundation, and the U.S. Department of Energy Office of Science. The SDSS-III web site is <http://www.sdss3.org/>. SDSS-III is managed by the Astrophysical Research Consortium for the Participating Institutions of the SDSS-III Collaboration including the University of Arizona, the Brazilian Participation Group, Brookhaven National Laboratory, Carnegie Mellon University, University of Florida, the French Participation Group, the German Participation Group, Harvard University, the Instituto de Astrofísica de Canarias, the Michigan State/Notre Dame/JINA Participation Group, Johns Hopkins University, Lawrence Berkeley National Laboratory, Max Planck Institute for Astrophysics, Max Planck Institute for Extraterrestrial Physics, New Mexico State University, New York University, Ohio State University, Pennsylvania State University, University of Portsmouth, Princeton University, the Spanish Participation Group, University of Tokyo, University of Utah, Vanderbilt University, University of Virginia, University of Washington, and Yale University. We acknowledge the Pan-STARRS Survey. The Pan-STARRS1 Surveys (PS1) and the PS1 public science archive have been made possible through contributions by the Institute for Astronomy, the University of Hawaii, the Pan-STARRS Project Office, the Max-Planck Society and its participating institutes, the Max Planck Institute for Astronomy, Heidelberg and the Max Planck Institute for Extraterrestrial Physics, Garching, The Johns Hopkins University, Durham University, the University of Edinburgh, the Queen's University Belfast, the Harvard-Smithsonian Center for Astrophysics, the Las Cumbres Observatory Global Telescope Network Incorporated, the National Central University of Taiwan, the Space Telescope Science Institute, the National Aeronautics and Space Administration under Grant No. NNX08AR22G issued through the Planetary Science Division of the NASA Science Mission Directorate, the National Science Foundation Grant No. AST-1238877, the University of Maryland, Eotvos Lorand University (ELTE), the Los Alamos National Laboratory, and the Gordon and Betty Moore Foundation.

## DATA AVAILABILITY

All data are incorporated into the article and its online supplementary material.

## REFERENCES

- Abbott T. M. C., Adamów M., Aguena M., Allam S., Amon A., Annis J., Avila S., et al., 2021, *ApJS*, 255, 20. doi:10.3847/1538-4365/ac00b3
- Abdollahi S., Acero F., Ackermann M., Ajello M., Atwood W. B., Axelsson M., Baldini L., et al., 2020, *ApJS*, 247, 33. doi:10.3847/1538-4365/ab6bcb
- Abdollahi S., Acero F., Baldini L., Ballet J., Bastieri D., Bellazzini R., Berenji B., et al., 2022, *ApJS*, 260, 53. doi:10.3847/1538-4365/ac6751
- Acero F., Donato D., Ojha R., Stevens J., Edwards P. G., Ferrara E., Blanchard J., et al., 2013, *ApJ*, 779, 133. doi:10.1088/0004-637X/779/2/133
- Acero F., Ackermann M., Ajello M., Albert A., Atwood W. B., Axelsson M., Baldini L., et al., 2015, *ApJS*, 218, 23. doi:10.1088/0067-0049/218/2/23
- Ackermann M., Ajello M., Allafort A., Antolini E., Baldini L., Ballet J., Barbiellini G., et al., 2012, *ApJ*, 753, 83. doi:10.1088/0004-637X/753/1/83
- Aharonian F. A., 2000, *NewA*, 5, 377. doi:10.1016/S1384-1076(00)00039-7

- Ahumada R., Allende Prieto C., Almeida A., Anders F., Anderson S. F., Andrews B. H., Anguiano B., et al., 2020, *ApJS*, 249, 3. doi:10.3847/1538-4365/ab929e
- Ajello M., Romani R. W., Gasparrini D., Shaw M. S., Bolmer J., Cotter G., Finke J., et al., 2014, *ApJ*, 780, 73. doi:10.1088/0004-637X/780/1/73
- Ajello M., Di Mauro M., Paliya V. S., Garrappa S., 2020, *ApJ*, 894, 88. doi:10.3847/1538-4357/ab86a6
- Ajello M., Angioni R., Axelsson M., Ballet J., Barbiellini G., Bastieri D., Becerra Gonzalez J., et al., 2020, *ApJ*, 892, 105. doi:10.3847/1538-4357/ab791e
- Ajello M., Baldini L., Ballet J., Bastieri D., Becerra Gonzalez J., Bellazzini R., Berretta A., et al., 2022, *ApJS*, 263, 24. doi:10.3847/1538-4365/ac9523
- Böttcher M., Reimer A., Zhang H., 2013, *EPJWC*, 61, 05003. doi:10.1051/epjconf/20136105003
- Bruzewski S., Schinzel F. K., Taylor G. B., Petrov L., 2021, *ApJ*, 914, 42. doi:10.3847/1538-4357/abf73b
- Cardelli J. A., Clayton G. C., Mathis J. S., 1989, *ApJ*, 345, 245. doi:10.1086/167900
- Casa Team et al., 2022, *PASP*, 134, 1041. doi:10.1088/1538-3873/ac9642
- Cerruti M., Zech A., Boisson C., Inoue S., 2011, *sf2a.conf*, 555. doi:10.48550/arXiv.1111.0557
- Cerruti M., 2020, *JPhCS*, 1468, 012094. doi:10.1088/1742-6596/1468/1/012094
- Chambers K. C., Magnier E. A., Metcalfe N., Flewelling H. A., Huber M. E., Waters C. Z., Denneau L., et al., 2016, *arXiv*, arXiv:1612.05560. doi:10.48550/arXiv.1612.05560
- Costamante L., Cutini S., Tosti G., Antolini E., Tramacere A., 2018, *MNRAS*, 477, 4749. doi:10.1093/mnras/sty887
- Coziol R., Andernach H., Torres-Papaqui J. P., Ortega-Minakata R. A., Moreno del Rio F., 2017, *MNRAS*, 466, 921. doi:10.1093/mnras/stw3164
- Das S., Gupta N., Razaque S., 2022, *icrc.conf*, 1002. doi:10.22323/1.395.01002
- D’Abrusco R., Massaro F., Paggi A., Masetti N., Tosti G., Giroletti M., Smith H. A., 2013, *ApJS*, 206, 12. doi:10.1088/0067-0049/206/2/12
- de Menezes R., Peña-Herazo H. A., Marchesini E. J., D’Abrusco R., Masetti N., Nemmen R., Massaro F., et al., 2019, *A&A*, 630, A55. doi:10.1051/0004-6361/201936195
- Desai A., Marchesi S., Rajagopal M., Ajello M., 2019, *ApJS*, 241, 5. doi:10.3847/1538-4365/ab01fc
- Doert M., Errando M., 2014, *ApJ*, 782, 41. doi:10.1088/0004-637X/782/1/41
- Evans P. A., Beardmore A. P., Page K. L., Osborne J. P., O’Brien P. T., Willingale R., Starling R. L. C., et al., 2009, *MNRAS*, 397, 1177. doi:10.1111/j.1365-2966.2009.14913.x
- Evans P. A., Page K. L., Osborne J. P., Beardmore A. P., Willingale R., Burrows D. N., Kennea J. A., et al., 2020, *ApJS*, 247, 54. doi:10.3847/1538-4365/ab7db9
- Falcone A., Stroh M., Pryal M., 2014, *AAS*
- Falomo R., Pian E., Treves A., 2014, *A&ARv*, 22, 73. doi:10.1007/s00159-014-0073-z
- Fronte L., Mazzone B., Metruccio F., Munaretto N., Doro M., Giommi P., Viale I., et al., 2023, *JPhCS*, 2429, 012045. doi:10.1088/1742-6596/2429/1/012045
- Gao S., Fedynitch A., Winter W., Pohl M., 2019, *NatAs*, 3, 88. doi:10.1038/s41550-018-0610-1
- Garofalo D., Singh C. B., Walsh D. T., Christian D. J., Jones A. M., Zack A., Webster B., et al., 2019, *RAA*, 19, 013. doi:10.1088/1674-4527/19/1/13
- Ghisellini G., Righi C., Costamante L., Tavecchio F., 2017, *MNRAS*, 469, 255. doi:10.1093/mnras/stx806
- Giommi P., Glauch T., Padovani P., Resconi E., Turcati A., Chang Y. L., 2020, *MNRAS*, 497, 865. doi:10.1093/mnras/staa2082
- Giroletti M., Massaro F., D’Abrusco R., Lico R., Burlon D., Hurley-Walker N., Johnston-Hollitt M., et al., 2016, *A&A*, 588, A141. doi:10.1051/0004-6361/201527817
- Goad M. R., Tyler L. G., Beardmore A. P., Evans P. A., Rosen S. R., Osborne J. P., Starling R. L. C., et al., 2007, *A&A*, 476, 1401. doi:10.1051/0004-6361:20078436
- Gordon Y. A., Boyce M. M., O’Dea C. P., Rudnick L., Andernach H., Vantghem A. N., Baum S. A., et al., 2021, *ApJS*, 255, 30. doi:10.3847/1538-4365/ac05c0
- Gürkan G., Hardcastle M. J., Best P. N., Morabito L. K., Prandoni I., Jarvis M. J., Duncan K. J., et al., 2019, *A&A*, 622, A11. doi:10.1051/0004-6361/201833892
- Hale C. L., McConnell D., Thomson A. J. M., Lenc E., Heald G. H., Hotan A. W., Leung J. K., et al., 2021, *PASA*, 38, e058. doi:10.1017/pasa.2021.47
- HI4PI Collaboration, Ben Bekhti N., Flöer L., Keller R., Kerp J., Lenz D., Winkel B., et al., 2016, *A&A*, 594, A116. doi:10.1051/0004-6361/201629178
- Järvelä E., Berton M., Crepaldi L., 2021, *FrASS*, 8, 147. doi:10.3389/frspas.2021.735310
- Joffre S., Silver R., Rajagopal M., Ajello M., Torres-Albà N., Pizzetti A., Marchesi S., et al., 2022, *ApJ*, 940, 139. doi:10.3847/1538-4357/ac9797
- Kaur A., Falcone A. D., Stroh M. D., Kennea J. A., Ferrara E. C., 2019, *ApJ*, 887, 18. doi:10.3847/1538-4357/ab4ceb
- Kaur A., Kerby S., Falcone A. D., 2023, *ApJ*, 943, 167. doi:10.3847/1538-4357/ac8b80
- Kellermann K. I., Sramek R., Schmidt M., Shaffer D. B., Green R., 1989, *AJ*, 98, 1195. doi:10.1086/115207
- Kerby S., Kaur A. D., Eskenasy R., Hancock F., Stroh M. C., Ferrara E. C., et al., 2021, *ApJ*, 923, 75. doi:10.3847/1538-4357/ac2e91
- Komossa S., 2008, *RMxAC*, 32, 86. doi:10.48550/arXiv.0710.3326
- Landi R., Bassani L., Stephen J. B., Masetti N., Malizia A., Ubertini P., 2015, *A&A*, 581, A57. doi:10.1051/0004-6361/201526221
- Mannheim K., 1993, *A&A*, 269, 67. doi:10.48550/arXiv.astro-ph/9302006
- Maraschi L., Ghisellini G., Celotti A., 1992, *ApJL*, 397, L5. doi:10.1086/186531
- Marcha M. J. M., Browne I. W. A., Impey C. D., Smith P. S., 1996, *MNRAS*, 281, 425. doi:10.1093/mnras/281.2.425
- Marchesi S., Kaur A., Ajello M., 2018, *AJ*, 156, 212. doi:10.3847/1538-3881/aae201
- Marchesini E. J., Paggi A., Massaro F., Masetti N., D’Abrusco R., Andruchow I., 2020, *A&A*, 638, A128. doi:10.1051/0004-6361/201936928
- Marchesini E. J., Reynaldi V., Vieyro F., Saponara J., Andruchow I., López I. E., Benaglia P., et al., 2023, *A&A*, 670, A91. doi:10.1051/0004-6361/202244899
- Massaro F., Landoni M., D’Abrusco R., Milisavljevic D., Paggi A., Masetti N., Smith H. A., et al., 2015, *A&A*, 575, A124. doi:10.1051/0004-6361/201425119
- Massaro F., Álvarez Crespo N., D’Abrusco R., Landoni M., Masetti N., Ricci F., Milisavljevic D., et al., 2016, *Ap&SS*, 361, 337. doi:10.1007/s10509-016-2926-6
- Massaro F., Marchesini E. J., D’Abrusco R., Masetti N., Andruchow I., Smith H. A., 2017, *ApJ*, 834, 113. doi:10.3847/1538-4357/834/2/113
- Mirabal N., Frías-Martínez V., Hassan T., Frías-Martínez E., 2012, *MNRAS*, 424, L64. doi:10.1111/j.1745-3933.2012.01287.x
- Monet D. G., Levine S. E., Canzian B., Ables H. D., Bird A. R., Dahn C. C., Guetter H. H., et al., 2003, *AJ*, 125, 984. doi:10.1086/345888
- Monroe T. R., Prochaska J. X., Tejos N., Worseck G., Hennawi J. F., Schmidt T., Tumlinson J., et al., 2016, *AJ*, 152, 25. doi:10.3847/0004-6256/152/1/25
- Murase K., Oikonomou F., Petropoulou M., 2018, *ApJ*, 865, 124. doi:10.3847/1538-4357/aada00
- Neeleman M., Prochaska J. X., Ribaldo J., Lehner N., Howk J. C., Rafelski M., Kanekar N., 2016, *yCat*, *JApJ*/818/113. doi:10.26093/cds/vizier.18180113
- Nolan P. L., Abdo A. A., Ackermann M., Ajello M., Allafort A., Antolini E., Atwood W. B., et al., 2012, *ApJS*, 199, 31. doi:10.1088/0067-0049/199/2/31
- Nori M., Giroletti M., Massaro F., D’Abrusco R., Paggi A., Tosti G., Funk S., 2014, *ApJS*, 212, 3. doi:10.1088/0067-0049/212/1/3
- Osterbrock D. E., 1980, *NYASA*, 336, 22. doi:10.1111/j.1749-6632.1980.tb15916.x
- Padovani P., Alexander D. M., Assef R. J., De Marco B., Giommi P., Hickox R. C., Richards G. T., et al., 2017, *A&ARv*, 25, 2. doi:10.1007/s00159-017-0102-9
- Padovani P., Giommi P., Falomo R., Oikonomou F., Petropoulou

- M., Glauch T., Resconi E., et al., 2022, MNRAS, 510, 2671. doi:10.1093/mnras/stab3630
- Paiano S., Landoni M., Falomo R., Treves A., Scarpa R., Righi C., 2017, ApJ, 837, 144. doi:10.3847/1538-4357/837/2/144
- Paiano S., Landoni M., Falomo R., Treves A., Scarpa R., 2017, ApJ, 844, 120. doi:10.3847/1538-4357/aa7aac
- Paiano S., Franceschini A., Stamerra A., 2017, MNRAS, 468, 4902. doi:10.1093/mnras/stx749
- Paiano S., Falomo R., Franceschini A., Treves A., Scarpa R., 2017, ApJ, 851, 135. doi:10.3847/1538-4357/aa9af4
- Paiano S., Falomo R., Treves A., Franceschini A., Scarpa R., 2019, ApJ, 871, 162. doi:10.3847/1538-4357/aa6fe4
- Paiano S., Falomo R., Treves A., Scarpa R., 2020, MNRAS, 497, 94. doi:10.1093/mnras/staa1840
- Paiano S., Falomo R., Treves A., Padovani P., Giommi P., Scarpa R., 2021, MNRAS, 504, 3338. doi:10.1093/mnras/stab1034
- Paiano S., Falomo R., Treves A., Padovani P., Giommi P., Scarpa R., Bisogni S., et al., 2023, MNRAS, 521, 2270. doi:10.1093/mnras/stad573
- Pajdosz-Śmierciak U., Śmierciak B., Jamroz M., 2022, MNRAS, 514, 2122. doi:10.1093/mnras/stac1372
- Paliya V. S., Dominguez A., Ajello M., Olmo-Garcia A., Hartmann D., 2021, yCat, JApJS/253/46
- Perlmutter S., 2000, IJMPA, 15, 715. doi:10.1142/S0217751X00005383
- Petrov L., Mahony E. K., Edwards P. G., Sadler E. M., Schinzel F. K., McConnell D., 2013, MNRAS, 432, 1294. doi:10.1093/mnras/stt550
- Rakshit S., Stalín C. S., Chand H., Zhang X.-G., 2017, ApJS, 229, 39. doi:10.3847/1538-4365/aa6971
- Rajagopal M., Marchesi S., Kaur A., Domínguez A., Silver R., Ajello M., 2021, ApJS, 254, 26. doi:10.3847/1538-4365/abf656
- Rajagopal M., Marcotulli L., Labrie K., Marchesi S., Ajello M., 2023, AJ, 165, 42. doi:10.3847/1538-3881/aca1be
- Rodrigues X., Gao S., Fedynitch A., Palladino A., Winter W., 2019, ApJL, 874, L29. doi:10.3847/2041-8213/ab1267
- Romani R. W., Kerr M., Craig H. A., Johnston S., Cognard I., Smith D. A., 2011, ApJ, 738, 114. doi:10.1088/0004-637X/738/1/114
- Rusinek-Abarca K., Sikora M., 2021, ApJ, 922, 202. doi:10.3847/1538-4357/ac2429
- Salvetti D., Mignani R. P., De Luca A., Marelli M., Pallanca C., Breeveld A. A., Hüsemann P., et al., 2017, MNRAS, 470, 466. doi:10.1093/mnras/stx1247
- Salvetti D., Chiaro G., La Mura G., Thompson D. J., 2017, MNRAS, 470, 1291. doi:10.1093/mnras/stx1328
- Sbarufatti B., Treves A., Falomo R., Heidt J., Kotilainen J., Scarpa R., 2005, AJ, 129, 559. doi:10.1086/427138
- Schinzel F. K., Petrov L., Taylor G. B., Mahony E. K., Edwards P. G., Kovalev Y. Y., 2015, ApJS, 217, 4. doi:10.1088/0067-0049/217/1/4
- Schinzel F. K., Petrov L., Taylor G. B., Edwards P. G., 2017, ApJ, 838, 139. doi:10.3847/1538-4357/aa6439
- Seehars S., Grandis S., Amara A., Refregier A., 2016, PhRvD, 93, 103507. doi:10.1103/PhysRevD.93.103507
- Shaw M. S., Romani R. W., Healey S. E., Cotter G., Michelson P. F., Readhead A. C. S., 2009, ApJ, 704, 477. doi:10.1088/0004-637X/704/1/477
- Shaw M. S., Romani R. W., Cotter G., Healey S. E., Michelson P. F., Readhead A. C. S., Richards J. L., et al., 2012, ApJ, 748, 49. doi:10.1088/0004-637X/748/1/49
- Shaw M. S., Romani R. W., Cotter G., Healey S. E., Michelson P. F., Readhead A. C. S., Richards J. L., et al., 2013, ApJ, 764, 135. doi:10.1088/0004-637X/764/2/135
- Shimwell T. W., Hardcastle M. J., Tasse C., Best P. N., Röttgering H. J. A., Williams W. L., Botteon A., et al., 2022, A&A, 659, A1. doi:10.1051/0004-6361/202142484
- Stephen J. B., Bassani L., Landi R., Malizia A., Sguera V., Bazzano A., Masetti N., 2010, MNRAS, 408, 422. doi:10.1111/j.1365-2966.2010.17123.x
- Stroh M. C., Falcone A. D., 2013, ApJS, 207, 28. doi:10.1088/0067-0049/207/2/28
- Takahashi Y., Kataoka J., Nakamori T., Maeda K., Makiya R., Totani T., Cheung C. C., et al., 2012, ApJ, 747, 64. doi:10.1088/0004-637X/747/1/64
- Takeuchi Y., Kataoka J., Maeda K., Takahashi Y., Nakamori T., Tahara M., 2013, ApJS, 208, 25. doi:10.1088/0067-0049/208/2/25
- Urry C. M., Scarpa R., O'Dowd M., Falomo R., Pesce J. E., Treves A., 2000, ApJ, 532, 816. doi:10.1086/308616
- Uslenghi M., Falomo R., 2011, SPIE, 8135, 813524. doi:10.1117/12.913305
- Wang D.-L., Wang J.-G., Dong X.-B., 2009, RAA, 9, 1078. doi:10.1088/1674-4527/9/10/002

## APPENDIX A: X-RAY SKYMAPS

In the appendix the X-ray sky maps for the 33 UGS analysed in this paper are shown. The yellow and cyan ellipses are respectively the  $2\sigma$  and  $3\sigma$  *Fermi*  $\gamma$ -ray error regions. X-ray detection, found through *Swift*/XRT analysis, are reported in green.

**APPENDIX B: OPTICAL SKY MAPS**

In the appendix the optical skymaps for the 33 UGS analysed in this paper are shown. The green circle represent the error box of the X-ray counterpart and the red ellipses the error box of radio counterparts found or within VLASS, RACS or LoTSS catalogs.



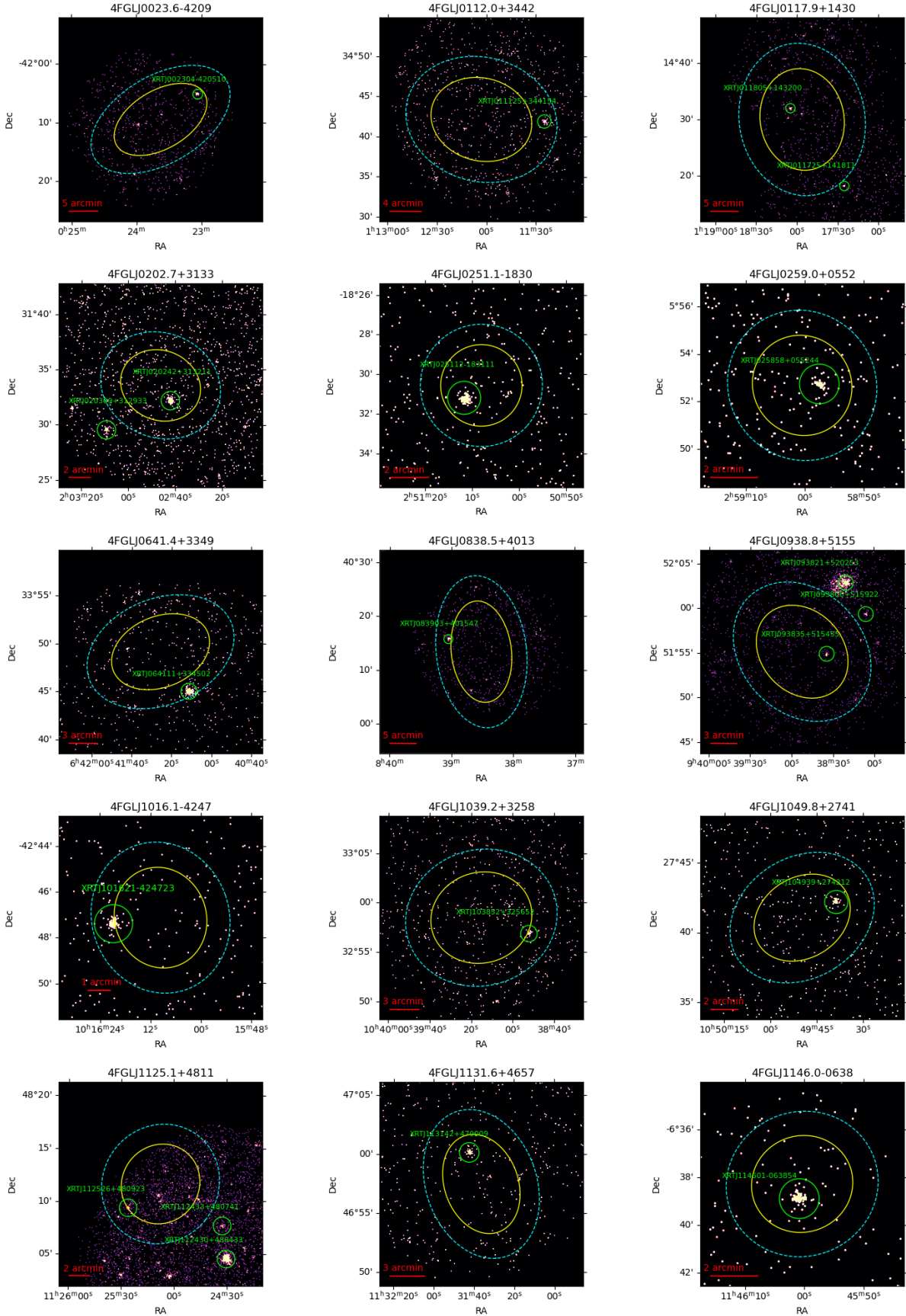


**Figure A1.** X-ray skymaps for 33 UGS. The yellow and cyan ellipses are respectively the  $2\sigma$  and  $3\sigma$  Fermi  $\gamma$ -ray error regions. X-ray detection, found through *Swift*/XRT analysis, are reported in green.

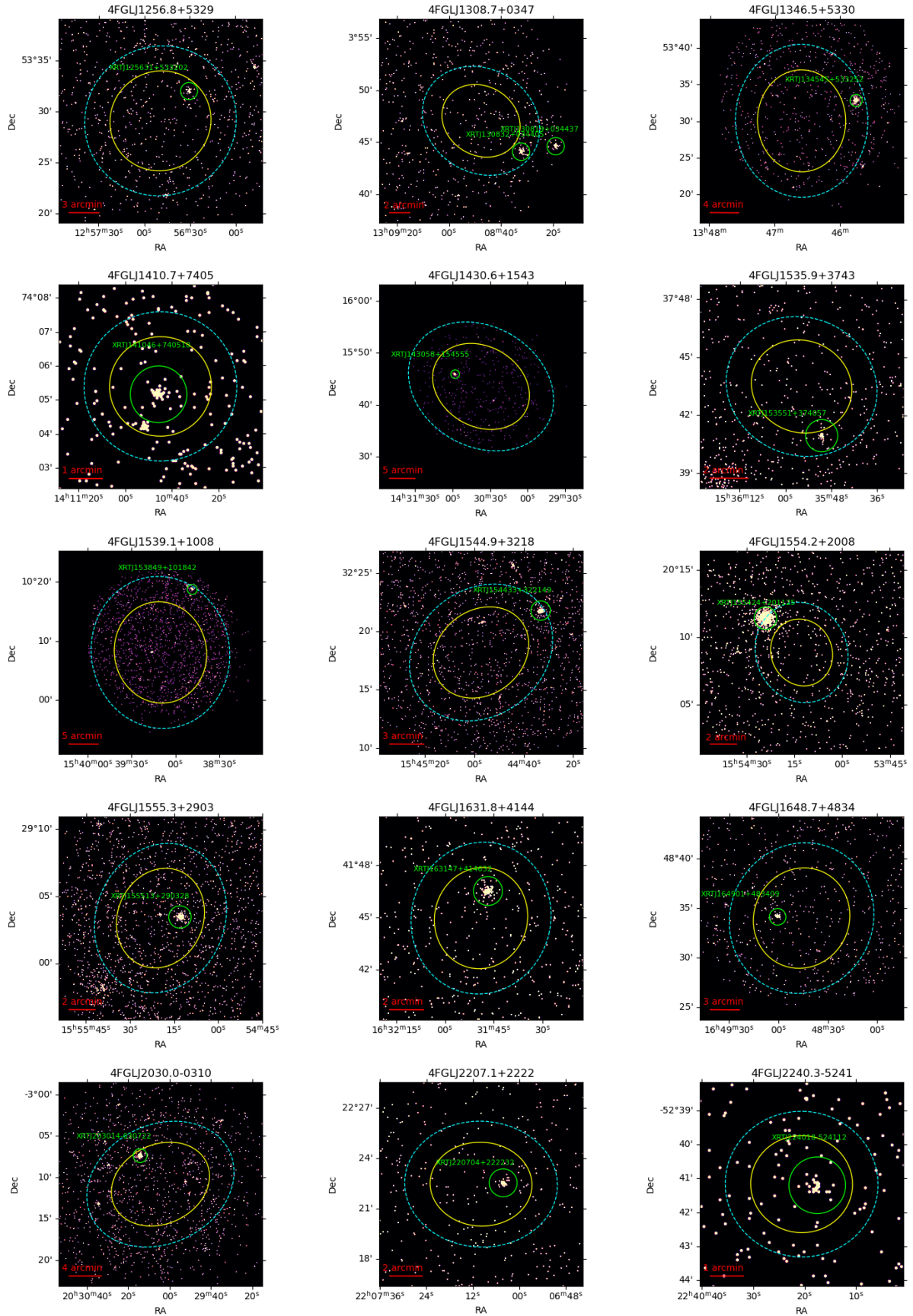


Figure A1. Continued

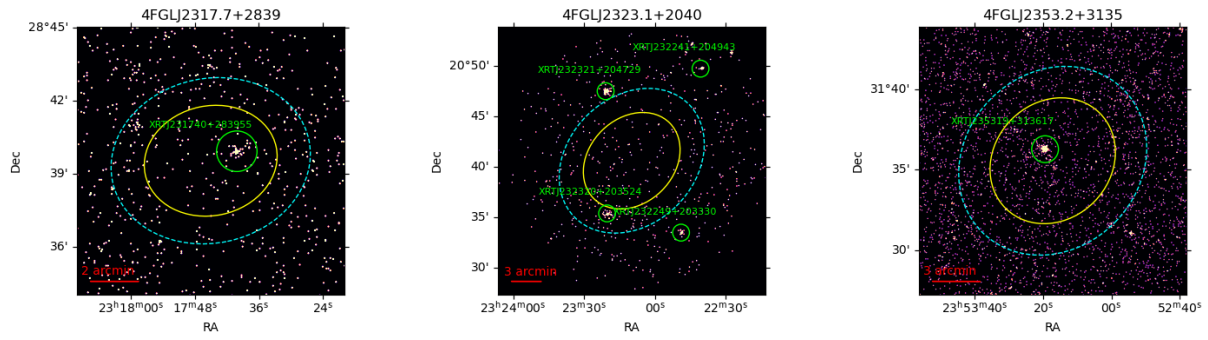
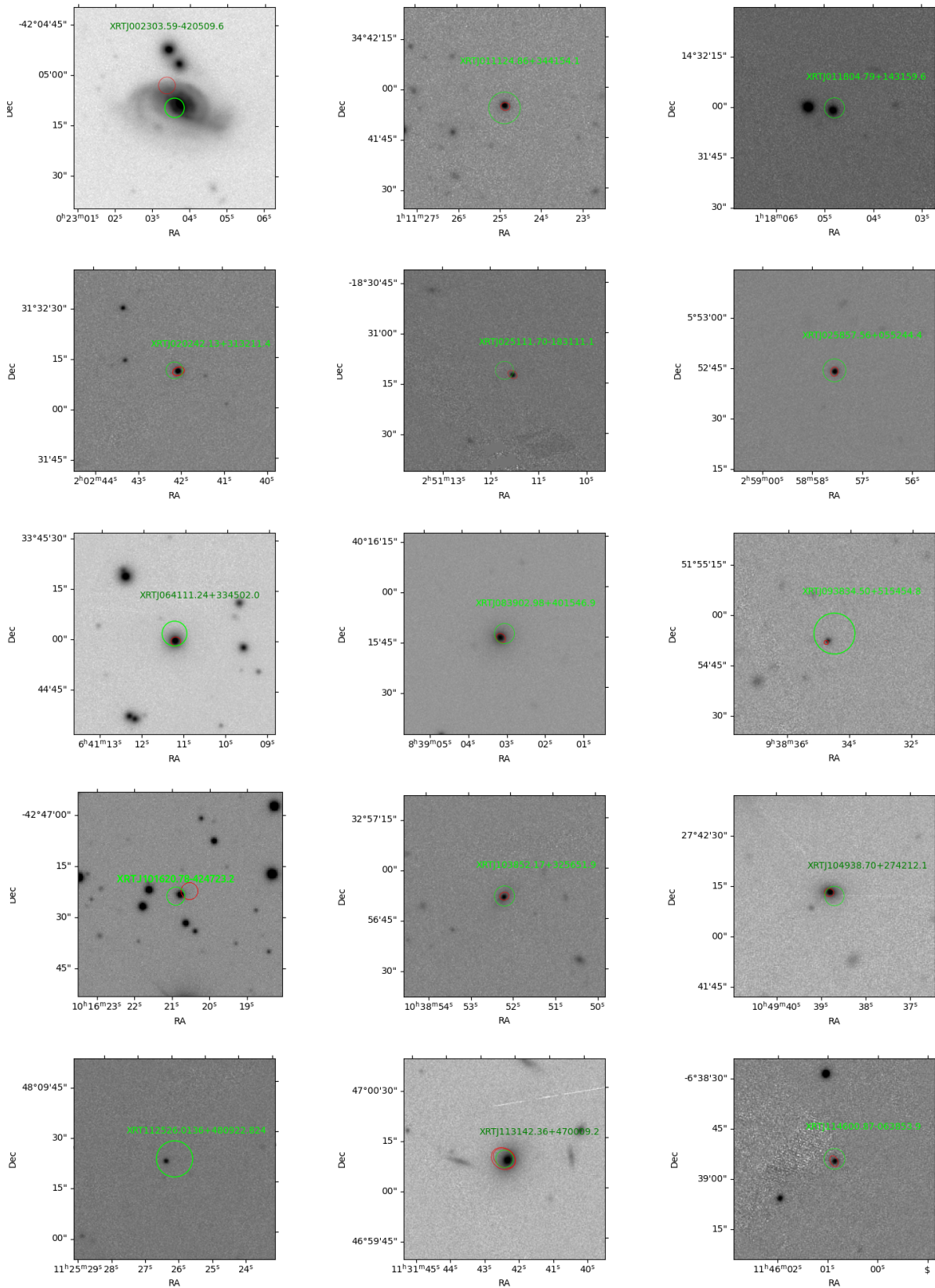


Figure A1. Continued



**Figure B2.** Optical r-band skymaps for 33 UGS counterparts. The green circle represent the error box of the X-ray counterpart and the red ellipses the error box of radio counterparts found or within VLASS, RACS or LoTSS catalogs.

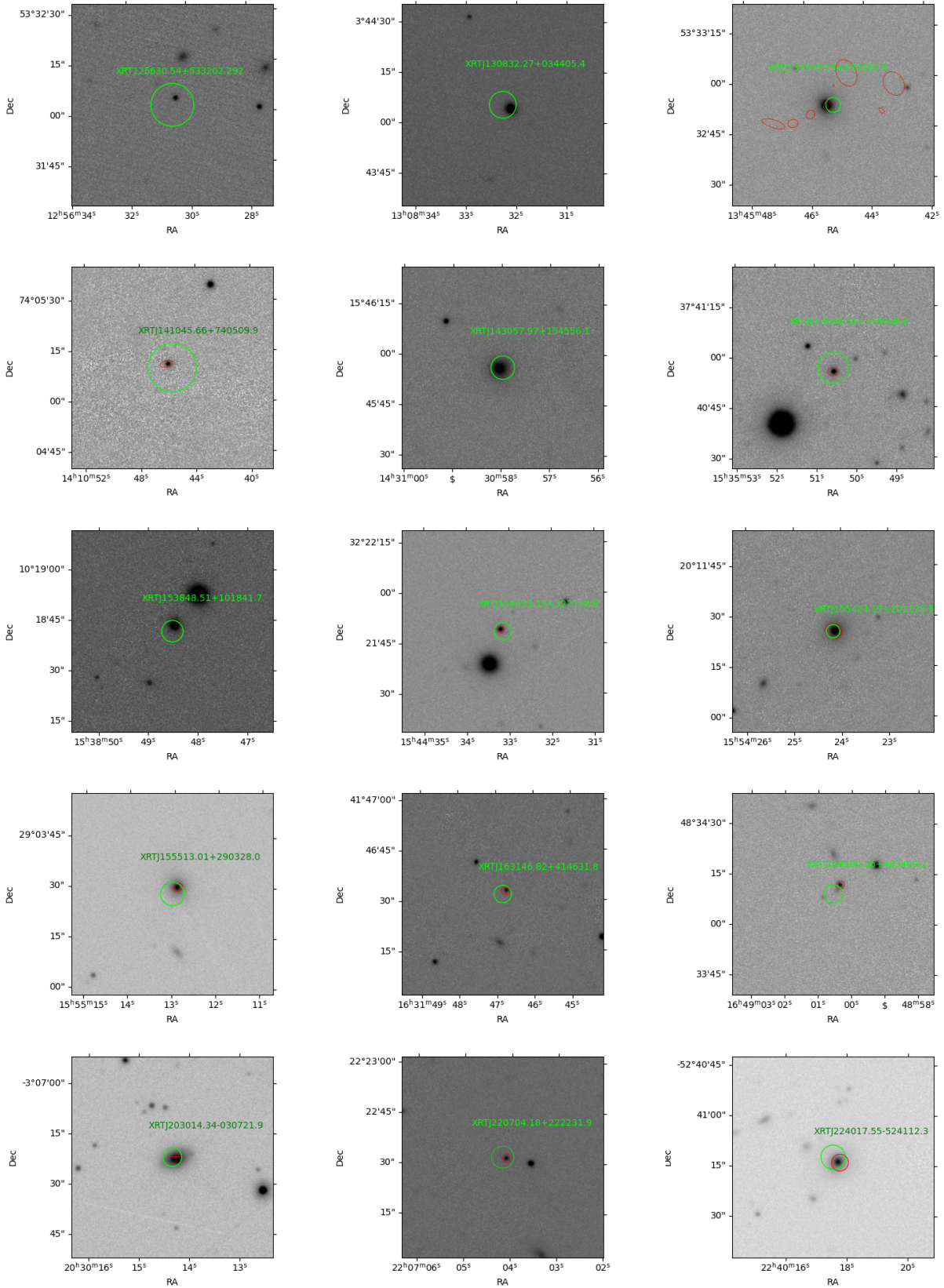
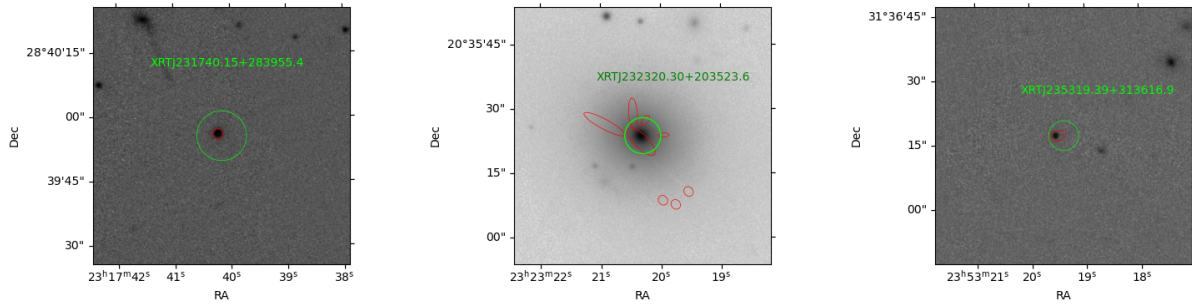


Figure B2. Continued.



**Figure B2.** Continued